Universidad de Sevilla

Facultad de Física

Fast-ion transport induced by externally applied Resonant Magnetic Perturbations in the ASDEX Upgrade tokamak

Author:
Lucía Sanchís

Supervisor:
Dr. Manuel García Muñoz
Dr. Antti Snicker

A thesis submitted in fulfillment of the requirements
for the degree of Doctor of Philosophy

in the

Plasma Science and Fusion Technology Group
Department of Atomic, Molecular and Nuclear Physics

June, 2019

Abstract

In magnetically confined fusion plasmas, MHD instabilities such as the Edge Localized Modes (ELMs), present in current devices, need to be kept under control in order to avoid too high heat fluxes on plasma facing components. Therefore, substantial efforts have been focused on developing techniques to mitigate these instabilities. Among these methods, one of the most promising techniques is the application of external Magnetic Perturbations (MPs), which have been observed to effectively mitigate or even suppress ELM instabilities. However, the inclusion of a 3D perturbative field has a strong impact on the plasma stability and confinement.

Fast-ions (i.e. supra-thermal ions) resulting from the fusion device plasma heating systems and fusion reactions require a good confinement to preserve the device performance and integrity. Therefore, the study of the impact that perturbative fields have on energetic particles is crucial to assess and design the MPs systems in future machines like ITER.

In this thesis, dedicated experiments in AUG have been carried out to analyse the fast-ion transport dependence on the poloidal spectra of the perturbation, showing that the amplitude of the observed fast-ion losses depends strongly on the energetic particle phase space and poloidal mode spectra of the external perturbation. The transport mechanism underlying these experimental results has been analysed through realistic numerical simulations using the ASCOT code. The results of these simulations have been combined with an analytical theory of nonlinear wave-particle resonances. This has shown that the combination of multiple linear and nonlinear resonances with the applied perturbative fields create a region where resonant transport is maximised. This transport occurs at the plasma edge and depends on the perturbation poloidal and toroidal spectra, as well as the magnetic equilibrium and

particle orbit topology. The impact of the collisionality and the radial electric fields on these resonances has also been assessed throughout this work. This analysis contributes to the ability to control the resonant transport at the plasma edge, which opens new avenues for the control of the energetic particle population and associated MHD fluctuations in future burning plasmas.

Contents

Chapter 1

Introduction

1.1 Fusion as energy source

To satisfy the energy demand derived from the current technological progress and increasing population, nuclear fusion appears as a clean energy source alternative to fossil fuel, which at present represents ≈80% of the global primary energy consumption [1]. The use of fossil fuel as the main energy source is not only restricted by the limited resources, but also by its capacity to increase dramatically the green house emission levels.

Nuclear fusion releases energy when two light nuclei combine into a heavier element following Einstein's famous mass relation. This process has been observed in nature as the way in which stars are fueled. In the sun, the energy is extracted from the conversion of two protons into helium through a three step fusion process called the proton-proton chain [2].

To achieve fusion, the reactants must overcome the Coulomb barrier. This issue is solved in the case of the stars by means of the large gravity forces caused by their huge masses. On the Earth, as it is impossible to reproduce the intensity of the gravity field, the solution involves heating the nuclei up to several keV. However, this alternative is limited by the reactivity of the nuclear processes. In figure 1.1 the cross sections of various reactions as a function of the kinetic energy are

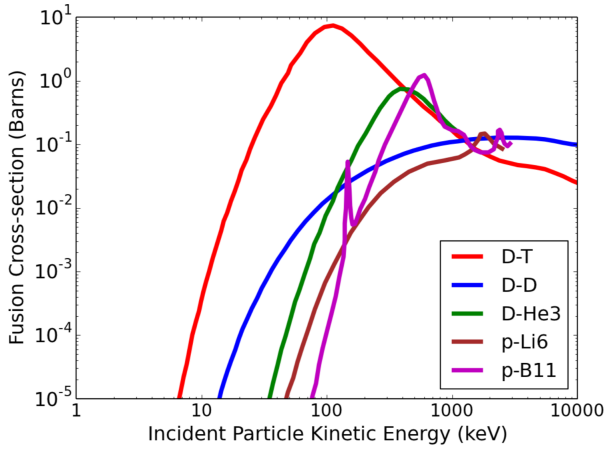

Figure 1.1: *Cross-sections corresponding to different fusion reactions as a function of the kinetic energy [3].*

shown. This indicates that the most promising reaction to reproduce on Earth is the $D + T \rightarrow H_e + n$, which releases 17.6 MeV of energy, reaction as it has the largest reactivity at the lowest energy.

The D-T reaction is not only the most favourable one in terms of reaction rate, but also regarding the availability of the reactants. Deuterium is abundant on earth and can be found in sea water. Tritium is more rare, but can be obtained from *Li* and the resulting neutrons from the D-T reaction. The neutrons produced in the D-T reaction carry most of the energy released, so they can also be used to boil water into steam to generate electricity.

At the high temperatures required to achieve fusion reactions, the matter is in a ionised state dominated by collective phenomena and self-organised called *plasma*. To achieve controlled fusion on earth as a viable energy source, the power balance of the process must be positive, i.e. the energy released from the fusion reaction must be higher than the energy provided to heat the plasma, taking into account that the conversion process of energy released into useful energy entails additional losses. If the energy provided by the fusion reaction itself is enough to maintain the fusion processes without any external input power, the plasma is said to *ignite* and the nuclear reactions become self-sustained. However, the sustainability of an ignited

plasma requires a good confinement of the plasma. The conditions which must be fulfilled in a fusion reaction volume to guarantee a positive power balance are given by the triple product [4]:

$$T \cdot n \cdot \tau_E > 3 \times 10^{21}\, m^{-3}\, keV\, s \tag{1.1}$$

for D-T reactions, where T is the plasma temperature, n is the plasma density and τ_E is the energy confinement time, defined as ratio between the plasma energy and the power loss. This criterion provides a measure of the feasibility of a certain plasma confinement system from the perspective of achieving plasma ignition.

In order to accomplish fusion reactions in hot plasmas, a good confinement of the matter is essential as the probability of elastic Coulomb interactions is higher than fusion reactions. Since the 1950s this problem has been approached through different methods that fall into two main categories: inertial and magnetic confinement.

- Intertial confinement:

  In this confinement approach, a capsule of fuel is heated and compressed by a powerful laser until the fusion reaction burns the fuel. In this process, the reactants are confined by its own inertia and the confinement time only lasts for a very short time, on the order of microseconds.

- Magnetic confinement:

  As the plasma consists of ionised particles, in the presence of a magnetic field their trajectories are tied to the magnetic field lines by the Lorentz force. Magnetic devices usually have a toroidal symmetry to ensure closed magnetic field lines and therefore, restrict the ion trajectories. However, as will be discussed later, this toroidal geometry is not enough to ensure the confinement of particles.

1.2 Tokamaks and the role of fast-ions

Among all different approaches to provide sufficient confinement to accomplish controlled fusion, the most developed concept is the tokamak. A tokamak is a toroidal

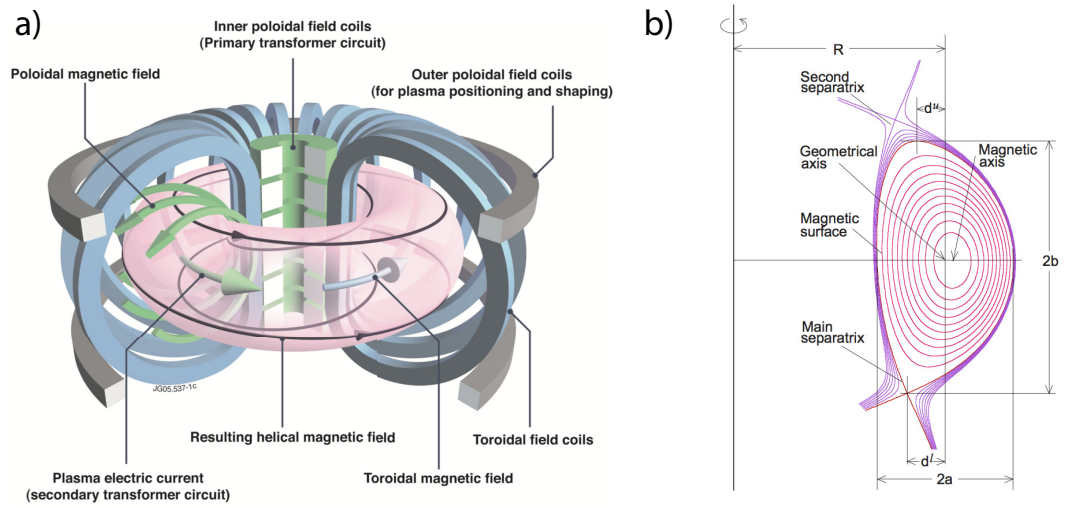

Figure 1.2: *a) Sketch of the main components of a tokamak device. The total magnetic field (black lines) consist of a poloidal field (green arrows) generated by the plasma current and a toroidal field (blue arrow) generated by the toroidal field coils (blue). b) Poloidal cross section of a tokamak showing the constant flux surfaces of a magnetic equilibrium indicating the separatrix as the boundary between closed and open magnetic field lines.*

fusion device based on magnetic confinement that combines a toroidal magnetic field (blue arrow in Fig. 1.2 a)) and a poloidal magnetic field (green arrows in Fig. 1.2 a)). The toroidal field is generated by a set of toroidal coils (blue coils in Fig. 1.2 a)) that results in a magnetic field that depends on the distance to the device toroidal axis with $1/R$. However, this toroidal field is not capable of confining charged particles by itself due to the orbits drifts caused by the magnetic gradient ∇B. To overcome this issue, a primary transformer coil in the centre of the device (green coils in Fig. 1.2 a)) induces a toroidal current in the plasma that acts as the secondary transformer circuit and generates a poloidal field (green arrows in Fig. 1.2 a)). The combination of the poloidal and toroidal magnetic fields forms the resulting helical magnetic field of a tokamak (black arrows in Fig. 1.2 a)).

Figure 1.2 b) shows the poloidal cross section of a typical tokamak divertor plasma. This configuration aims to keep the plasma away from the main wall and concentrate the plasma wall interaction volume to a dedicated area called divertor. In figure 1.2 b), the contours represent the constant flux surfaces associated to closed magnetic field lines (red) and open field lines (magenta). The value associated to each con-

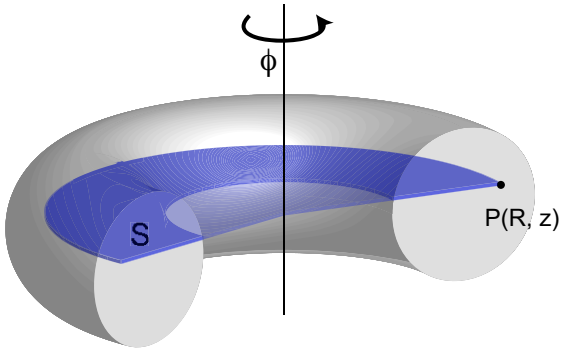

Figure 1.3: *Sketch showing the surface S used to define the poloidal magnetic flux* Ψ_{pol}.

tour is calculated as the flux of the poloidal magnetic field intersecting a surface of revolution along the toroidal axis S that connects each point to the magnetic axis:

$$\Psi_{pol} = \int \mathbf{B} \cdot d\mathbf{S} \tag{1.2}$$

Figure 1.3 shows the surface S (blue) to define the poloidal flux associated to a given (R, z) position. The poloidal flux is not dependent on the toroidal coordinate and is commonly used as a radial coordinate (ψ_{pol}). In this work, a normalised function of ψ_{pol} is used as a generalised radial coordinate defined as:

$$\rho_{pol} = \sqrt{\frac{\psi_{pol} - \psi_{axis}}{\psi_{sep} - \psi_{axis}}} \tag{1.3}$$

where ψ_{sep} and ψ_{axis} are the poloidal flux values evaluated at the last magnetic closed surface (separatrix) and at the magnetic axis, respectively.

The helicity of the magnetic field lines is one of the main characteristics of the magnetic equilibrium in a tokamak and can be related to the plasma stability. The evaluation of the helicity is given by the $safety\ factor$ defined as [5]:

$$q(\rho_{pol}) = \frac{1}{2\pi} \int_0^{2\pi} \left(\frac{rB_\phi}{RB_\theta} \right)_{\rho_{pol}} d\theta \tag{1.4}$$

evaluated at the corresponding constant ρ_{pol} surface. The safety factor is a function of the radial coordinate ρ_{pol} and represents the number of toroidal turns of a

field line to complete one poloidal turn.

The tokamak is presented as a device capable of confining hot plasmas through magnetic fields. However, to achieve the plasma conditions required to produce fusion reactions, the plasma needs to be heated up to several keV by means of different sources:

- The induced **plasma current** produces ohmic heating via the Joule effect. This method is only effective to heat the plasma up to temperatures in the order of keV since the resistivity of the plasma limits the dissipated energy [4, 6].
- Electron/Ion cyclotron resonant heating (**ECRH/ICRH**) systems use radio frequencies to accelerate electrons/ions whose cyclotron frequencies are in the vicinity of the radiofrequency.
- The **injection** of a high energy **beam** of **neutral** particles (**NBI**), which ionise and transfer part of their energy to the bulk plasma through Coulomb collisions.
- Energetic α particles released in the D-T reaction which transfer their energy through Coulomb collisions.

The use of some of these heating systems is inherent to the generation of a new particle distribution with energies above the thermal plasma. This energetic population, usually referred to as *fast-ions*, plays an essential role in the performance of a tokamak as they carry large amounts of energy. A poor confinement of these particles can lead to a dramatic decrease of the tokamak efficiency by losing stored plasma energy. In addition, a localised release of fast-ions into the vessel walls can cause severe material damages.

1.3 Motivation and scope of this work

Toroidal symmetry is the basis of magnetic fusion devices. Nested flux surfaces and particle constants of motion ensure plasma confinement in toroidal magnetic

fusion devices. Symmetry breaking 3D fields can, however, be used to overcome some difficulties intrinsic to ideal toroidal geometries, modifying the overall plasma confinement and stability [7].

In tokamaks, 3D perturbative fields may be mandatory to preserve the device performance and possibly even integrity against intolerable plasma fluctuations that, if allowed to grow unabated, could damage the vacuum vessel though localised and intense particle losses [8–11].

The impact that externally applied 3D fields have on the overall plasma stability and confinement is, however, complicated by several simultaneous nonlinear effects that compete at different spatio-temporal scales [12, 13]. These effects include the magnetic equilibrium, main plasma parameters and perturbation mode spectra [14–17].

The fast-ion population is particularly affected by these perturbative fields as they have relatively long mean free paths and slowing-down times [18–25]. For the reasons stated above, energetic particles will be present in future fusion reactors as a part of the heating systems or as the product of the fusion reactions in the plasma. Therefore, the analysis of the fast-ion population in the presence of perturbative fields needs to be fully assessed.

In this thesis, the fast-ion transport has been analysed in the presence of externally applied 3D magnetic perturbations through experimental data and numerical simulations. The experimental data showed a clear dependence of the fast-ion transport with the magnetic configuration of the perturbation. This result was analysed by means of numerical simulations carried out with the ASCOT code [26] which revealed the existence of a resonant interaction between the fast-ions and the magnetic perturbation. The obtained results both numerical and experimental have been supported by an analytical theory in the framework of linear and nonlinear resonant interactions, providing a consistent understanding of the energetic particle transport due to 3D magnetic perturbations.

1.4 Outline

The work presented in this thesis is structured as follows. Chapter 2 introduces the main theories and concepts used throughout this work regarding the general behaviour of fast-ions in tokamaks.

In chapter 3, a derivation of the analytical theory of linear wave-particle resonant interaction in presented. Thereafter, this formalism is extended to include nonlinear interactions by introducing a periodic perturbation in the analised particle trajectories.
Chapter 4 includes a description of the AUG focusing on the technical aspects related to the fast-ion sources and the generation of externally applied magnetic perturbations. The orbit following code ASCOT is introduced.

In chapter 5, a description of the set up for the dedicated experiment carried out in the AUG to analyse the fast-ion transport in the presence of a perturbed magnetic field is presented with the experimental data obtained. The results of chapter 3 are used here to identify the fast-ion transport observed in the numerical simulations as linear and nonlinear resonant interaction between the particles and the applied magnetic perturbation.

Chapter 6 presents the results of the numerical simulations of fast-ion transport carried out with the ASCOT code reproducing the behaviour observed in the experiment. The fast-ion transport is characterised in the framework of resonant wave-particle interactions through the variation of the toroidal canonical momentum analysing its dependence on the perturbation poloidal spectra, perturbation amplitude, Coulomb collisions and radial electric field. Finally, chapter 7 is dedicated to summarise and discuss the most relevant results of this work

Chapter 2

Fast-ions in tokamak

The analysis of fast-ion transport in plasmas is crucial to achieve controlled nuclear fusion on earth. In this chapter, fast-ions in tokamaks are fully characterised and the necessary concepts involved in this work are introduced. First, the main fast-ion sources are presented. Then, the equations of motion are described in detail, leading to the analysis of the orbits topologies. Finally, the most relevant transport mechanisms are presented, focusing on the wave-particle resonant transport as it constitutes the basis of this thesis.

2.1 External heating as source of fast-ions

In tokamaks, the burning plasma regime is reached by means of heating systems which can affect the fast-ion distribution in the plasma. These heating systems include external mechanisms including the NBI and ICRH, and fusion born products such as α particles in $D-T$ plasmas. In this section, a brief description of the main fast-ion sources is presented.

- Neutral beam injector (NBI)

  The operating principle of the NBI system consists of a high energy beam of neutral atoms, mostly deuterium or hydrogen with energies above 10 keV. This beam is accelerated externally and neutralised so atoms can penetrate into the plasma without being deflected by the magnetic field. Once the neutral is

injected, it follows a rectilinear path until it ionises through electron and ion collision and charge exchange processes with the thermal ions. Each ionisation method has different cross-sections that depend on the energy, but in total, the NBI birth distribution has an exponential decrease along its path. When a particle is ionised, it is confined by the magnetic field. It transfers its energy to the plasma through collisions thus, heating the plasma [27].

In order to accelerate the injected neutrals, initially charged particles are extracted from an ion source, then accelerated through an electric potential and finally neutralised. The ion sources do not only contain D and H, but also molecular species such as $H_2^+, H_3^+, D_2^+, D_3^+$, resulting into a final beam which contains energetic ions at energies E_0, $E_0/2$ and $E_0/3$, where E_0 is the main injection energy.

In the ASDEX Upgrade tokamak (AUG), the NBI system consists of two boxes at different toroidal locations and each one contains four beams with different injection geometries, which can be radial or tangential to the magnetic field. The initial fast-ion population generated by the NBI system is strongly anisotropic, localised along the injection direction as it is shown in figure 2.1 for AUG. Also, defining the particle pitch as the cosine between the total velocity and the direction of the magnetic field lines as

$$\Lambda = v_{\parallel}/v \tag{2.1}$$

the birth distribution has a clear preferred value of pitch determined by the injection geometry and the magnetic equilibrium, restricting the topology of the ion orbits. A detailed description of the orbit topologies is given in section 2.5.

- Ion Cyclotron Resonance Heating (ICRH)

  A charged particle in a magnetic field has a cyclotron motion perpendicular to the magnetic field lines. In the presence of external electromagnetic waves, the wave-particle interaction can result into the acceleration or deceleration of the ion depending on the phase coupling [28]. The ICRH system uses the resonant

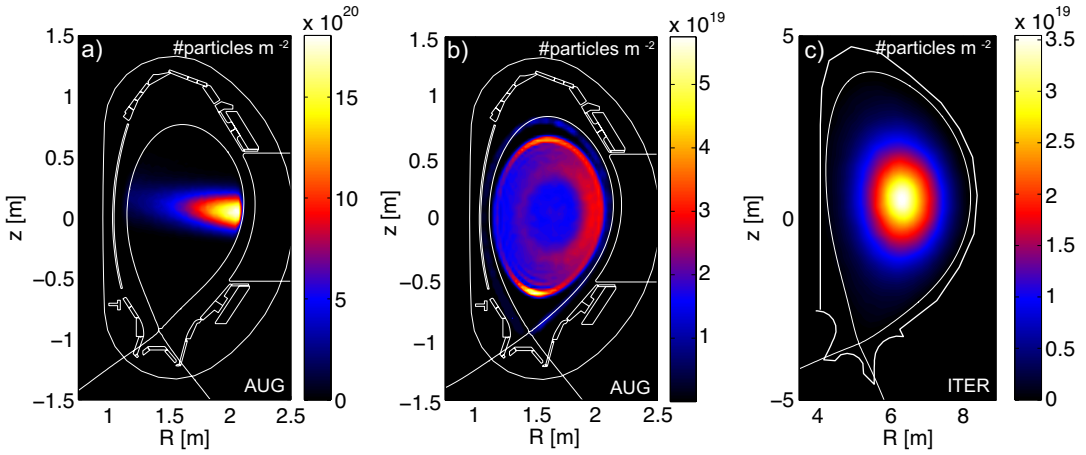

Figure 2.1: *2D histogram showing the surface density of the initial ion distribution projected onto the poloidal cross section for: a) NBI birth distribution in AUG. b) ICRH accelerated fast-ion distribution in AUG. c) Fusion born α particle distribution in ITER*

interaction between the rotating ions and electromagnetic waves defined by

$$\omega - k_{\parallel} v_{\parallel} - g\omega_c = 0 \tag{2.2}$$

to accelerate the plasma ions [29]. There, ω is the frequency of the external wave, ω_c is the cyclotron frequency, $k_{\parallel}$ is the parallel component of the wave vector, $v_{\parallel}$ is the parallel velocity and g is the mode number associated to the cyclotron frequency. In AUG, the electromagnetic waves are generated by a set of antennas using operation frequencies in the range of 30-90 MHz which can inject up to 6 MW power [30].

The fast-ion distribution resulting from the ICRH heating in AUG is shown in figure 2.1 b). The cyclotron frequency increases with the intensity of the magnetic field, considering that the magnetic field in a tokamak varies with the radius, a given resonant condition only affects a layer within a fixed radial location.

- Fusion-born products

  In tokamak plasmas, the fusion reactions release large amounts of energy. As presented in chapter 1.2, in future devices hosting $D + T$ reactions, energetic

α particles will be the main fast-ion source. The generation of α particles via fusion processes can happen through different reactions.

- Thermonuclear (target-target). Fusion reactions involving two ions from the bulk plasma.
- Beam-target. Fusion reactions between NBI ions and the bulk plasma.
- Beam-beam. Fusion reactions involving two NBI ions.

Figure 2.1 c) shows the α birth distribution due to thermonuclear reactions in ITER. In the thermonuclear case, the initial distribution of fusion-born products has a maximum in the centre as the density and temperatures are higher, which increases the reactivity of the fusion process.

2.2 Equations of motion

2.2.1 Full gyromotion

The time evolution of a charged particle in a electromagnetic field can be obtained from the Euler-Lagrange equations:

$$\frac{d}{dt}\left(\frac{\partial L}{\partial \dot{\mathbf{x}}}\right) = \left(\frac{\partial L}{\partial \mathbf{x}}\right) \tag{2.3}$$

where the noncanonical expression in cartesian coordinates is given by [31]:

$$L = \frac{m}{2}|\dot{\mathbf{x}}|^2 + e\dot{\mathbf{x}} \cdot A(\mathbf{x}, t) - e\Phi(\mathbf{x}, t) \tag{2.4}$$

with m and e are the particle mass and charge. The magnetic and electric fields are described through their vector $\mathbf{A}$ and scalar Φ potential respectively. Here the canonical momentum $\mathbf{p}$ can be defined as:

$$\mathbf{p} = \frac{\partial L}{\partial \dot{\mathbf{x}}} \tag{2.5}$$

$$\mathbf{p} = m\dot{\mathbf{x}} + e\mathbf{A} \tag{2.6}$$

Writing the hamiltonian through the Legendre transformation as a function of the phase-space coordinates ($\mathbf{x}$, $\mathbf{p}$):

$$H = \mathbf{p} \cdot \dot{\mathbf{x}} - L = \frac{1}{2m} |\mathbf{p} - e\mathbf{A}|^2 + e\Phi \tag{2.7}$$

where the particle velocity can be defined using equation 2.6 as:

$$v = \left(\frac{\mathbf{p} - e\mathbf{A}}{m} \right) : \tag{2.8}$$

This allows one to rewrite the langrangian as a function of variables ($\mathbf{x}$, $\dot{\mathbf{x}}$, $\mathbf{v}$, $\dot{\mathbf{v}}$):

$$L = \dot{\mathbf{p}}\mathbf{x} - H = \dot{\mathbf{p}}\mathbf{x} - \frac{1}{2m} |\mathbf{p} - e\mathbf{A}|^2 - e\Phi \tag{2.9}$$

$$L = (m\mathbf{v} + e\mathbf{A}) \cdot \dot{\mathbf{x}} - \left(e\Phi + \frac{m}{2} v^2 \right) \tag{2.10}$$

Using the Euler-Lagrange equations in each variable one can obtain:

$$\frac{d}{dt} \left(\frac{\partial L}{\partial \dot{\mathbf{v}}} \right) = \left(\frac{\partial L}{\partial \mathbf{v}} \right) \rightarrow \dot{\mathbf{x}} = \mathbf{v} \tag{2.11}$$

$$\frac{d}{dt} \left(\frac{\partial L}{\partial \dot{\mathbf{x}}} \right) = \left(\frac{\partial L}{\partial \mathbf{x}} \right) \rightarrow \frac{d}{dt} (m\mathbf{v} + e\mathbf{A}) = \nabla (e\mathbf{A} \cdot \dot{\mathbf{x}} - e\Phi) \tag{2.12}$$

Taking into account the expressions for the electromagnetic fields as a function of the scalar and vector potentials:

$$\mathbf{E} = -\frac{\partial \mathbf{A}}{\partial t} - \nabla\phi$$
$$\mathbf{B} = \nabla \times \mathbf{A}$$

equation can be rewritten as the Lorentz force:

$$m\dot{\mathbf{v}} = \mathbf{E} + e\dot{\mathbf{x}} \times \mathbf{B} \tag{2.13}$$

Equations 2.11 and 2.2.1 provide the time evolution of a particle considering the the full motion.

2.2.2 Guiding centre motion

According to equation 2.13, in the absence of an electric field, the Lorentz force is perpendicular to the particle velocity and the energy is conserved [32]. Figure 2.2 a) shows the resulting helical motion of the particle around the magnetic field lines which can be decomposed into parallel and perpendicular components $\mathbf{v} = v_{\parallel}\mathbf{b} + \mathbf{v}_{\perp}$, with $\mathbf{b}$ the unitary vector in the direction of the magnetic field. The parallel velocity $v_{\parallel}$ is constant as there is no force in this direction, while the perpendicular velocity $v_{\perp}$ describes a circular motion with frequency ω_c and gyroradious ρ:

$$\omega_c = \frac{|e|\,B}{m} \tag{2.14}$$

$$\rho = \frac{m v_{\perp}}{|e|\,B} \tag{2.15}$$

The ion trajectory can be decomposed into two different motions. Figure 2.2 b) shows the position of the ion as the superposition of the motion of the guiding centre ($\mathbf{R}$) and the Larmor radius (ρ). However, if the considered magnetic field has a slow time variation compared to the gyrofrequency of the ion (ω_c) and the spatial scale length is large compared to the gyroradius (ρ), the gyrophase is an ignorable coordinate and the magnetic moment μ is constant [33]. Here, the magnetic moment is the product of the current associated to the gyromotion ($e\omega_c/2\pi$) and the area encosed by ρ:

$$\mu = I \cdot A = \frac{e\omega_c}{2\pi} \cdot 2\pi\rho^2 = \frac{m v_{\perp}^2}{2B} \tag{2.16}$$

In this case, the guiding centre approach describes the trajectory of the particle ignoring its gyromotion. The guiding centre theory started as a nonhamiltoninan formulation [33, 34], but the errors derived from the lack of an energy conservation law motivated the development of a guiding centre hamiltonian theory [31]. The lagrangian of a charged particle in the guiding centre coordinates reads:

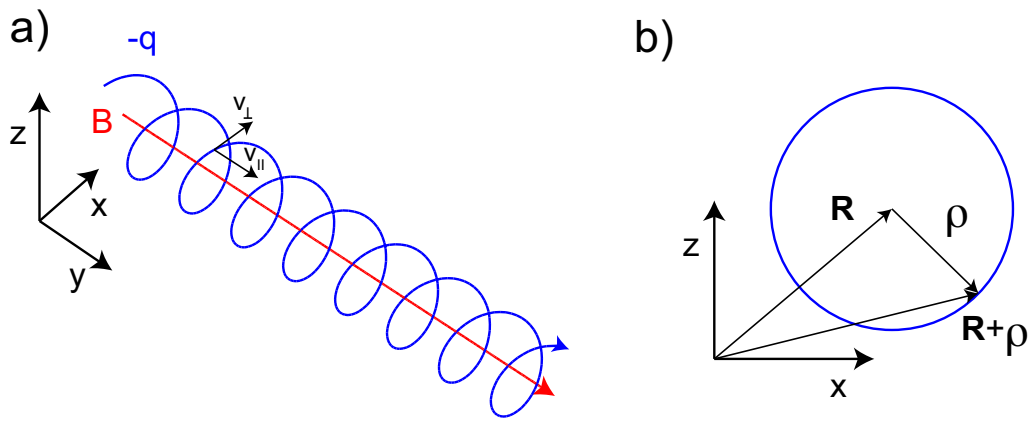

Figure 2.2: *a) Helical motion of an electron (blue) along the magnetic field lines (red). b) Decomposition of the particle location into guiding centre and gyromotion.*

$$L = (e\mathbf{A} + mv_{\parallel}\mathbf{b}) \cdot \dot{\mathbf{R}} + \frac{m\mu}{e}\dot{\chi} - H$$
$$H = \frac{1}{2}mv_{\parallel}^2 + \mu B + e\Phi$$

where $\mathbf{b}$ is a unit vector in the direction of the magnetic field and the gyrocentre is described by its magnetic moment as defined in equation 2.16, i.e. position, parallel velocity and gyrophase $(\mu, \mathbf{R}, v_{\parallel}, \chi)$. Using the Euler-Lagrange equation 2.3 it can be obtained that:

$$\dot{\mathbf{R}} = v_{\parallel}\frac{\mathbf{B}^*}{B_{\parallel}^*} + \mathbf{E}^* \times \frac{\mathbf{b}}{B_{\parallel}^*}$$
$$\dot{v_{\parallel}} = \frac{e}{m}\frac{\mathbf{B}^*}{B_{\parallel}^*} \cdot \mathbf{E}^*$$
$$\dot{\mu} = 0$$
$$\dot{\chi} = \frac{eB}{m}$$

with $B_{\parallel}^* = \mathbf{B}^* \cdot \mathbf{b}$ and the effective fields are given by:

$$\mathbf{E}^* = -\frac{\partial \mathbf{A}^*}{\partial t} - \nabla \phi^*$$
$$\mathbf{B}^* = \nabla \times \mathbf{A}^*$$
$$\Phi^* = \Phi + \frac{\mu B}{e}$$
$$\mathbf{A}^* = \mathbf{A} + \frac{m v_\parallel \mathbf{b}}{e}$$

Although this description is an approximation of the particle motion, it can result in large savings of computational resources when the approximation is valid.

2.3 Guiding centre particle drifts

Although the ASCOT code calculates the particle trajectories using the exact expression for the equations of motion in the hamiltonian formalism as it was described in section 2.2, for the sake of clarity, in this section the orbit drifts are presented in Northrop formulation [34] of the guiding centre motion to illustrate the drifts affecting a single particle in a tokamak. The exact expression for these drift can be found at [31].

In the presence of external forces $\mathbf{F}$ perpendicular to the magnetic field $\mathbf{B}$, a charged particle exhibits a drift which can be expressed through a velocity drift of the guiding centre given by:

$$\mathbf{v_{drift}} = \frac{1}{q}\frac{\mathbf{F} \times \mathbf{B}}{B^2} \tag{2.17}$$

In a tokamak, the drifts due to the toroidal magnetic configuration are the ∇B drift, the $E \times B$ drift and the curvature drift.

- ∇B drift

  Assuming that the magnetic field lines are straight but the intensity changes along one direction, the gyroradius of a given ion is smaller in the region where B is more intense according to equation 2.15. The periodic change in the

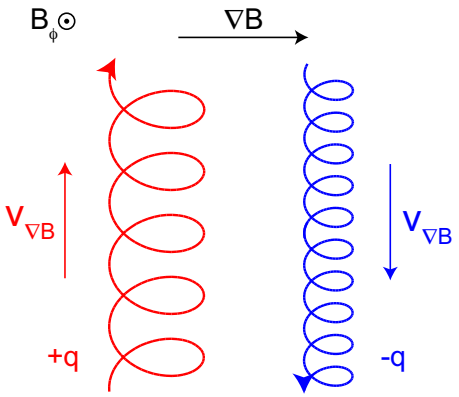

Figure 2.3: *Effect of $\nabla B \times B$ drift on ions and electrons.*

gyroradius leads to a particle drift that is perpendicular to the direction of the magnetic field and its gradient.

The force on a dipole caused by a variation in the magnetic field is given by:

$$\mathbf{F} = \mu \nabla B \tag{2.18}$$

where μ is the magnetic moment associate to the gyromotion. Combining equation 2.17 and 2.18, the drift velocity associated to the magnetic inhomogeneity yields:

$$\mathbf{v}_{\nabla \mathbf{B}} = \frac{m v_\perp^2}{2qB^3} \nabla B \times \mathbf{B} \tag{2.19}$$

From equation 2.16 it is clear that the direction of the drift depends on the sign of the charge so, in the presence of a ∇B, ions and electrons are forced into opposite directions, creating a charge separation and thus, inducing an electric field.

- Curvature drift

  If the intensity of the magnetic field is homogeneous but the magnetic field is curved by a constant radius (R_c), particles following the field lines experiment an outwards force caused by the lack of a centrifugal force to maintain the

curvature. The centrifugal force required to curve the ion trajectory along the magnetic field lines is:

$$\mathbf{F} = -\frac{mv_{\parallel}^2}{R_c^2}\mathbf{R_c} \tag{2.20}$$

Using equations 2.17 and 2.20, the curvature drift can be expressed as:

$$\mathbf{v_{R_c}} = \frac{mv_{\parallel}^2}{qR_c^2}\frac{\mathbf{R_c} \times B}{B^2} \tag{2.21}$$

Considering a typical toroidal magnetic field where the intensity of $\mathbf{B}$ decreases with the radius, both the curvature drift and the ∇B drift are in the same direction. Another similarity with the ∇B drift is the charge dependency, resulting into both drifts contributing to a charge separation.

- $E \times B$ drift

  In the presence of an electric field, charged particles exhibit a force in the direction of the field given by $\mathbf{F} = eZ\mathbf{E}$. From equation 2.17 it follows that:

$$\mathbf{v_{E\times B}} = \frac{\mathbf{E} \times \mathbf{B}}{B^2} \tag{2.22}$$

  This drift accelerates the particle, and therefore increases the gyroradius, when the velocity has a positive component in the same direction as $\mathbf{E} \times \mathbf{B}$ and decelerates, reducing the gyroradius, through the other half of the gyromotion. The periodic difference in the gyroradius results into a drift perpendicular to the applied electric field and independent of the charge as shown in figure 2.4.

2.4 Constants of motion and adiabatic invariants

In order to characterise a particle motion, it is common to make use of conserved quantities. Each symmetry in the motion of a system entails a conservation law, which means that an integral of motion exists [35]. In general, for each ignorable

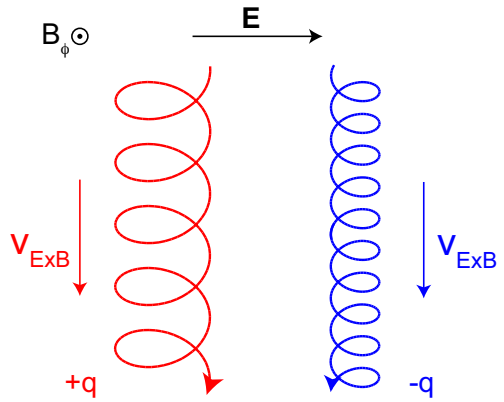

Figure 2.4: *Effect of $E \times B$ drift on ions and electrons.*

coordinate, the action $I = \oint P_x dx$ is kept constant, with P_x the canonical momentum associated to a given coordinate x.

Constants of motion:

- Energy

  In the absence of an electric field, the Lorentz force is always perpendicular to the particle displacement and the work done is zero. In this case, and considering a static magnetic field, the kinetic energy is an exact invariant.

$$E = \frac{1}{2}mv_\perp^2 + \frac{1}{2}mv_\parallel^2 = \mu B + \frac{1}{2}mv_\parallel^2 = const. \tag{2.23}$$

- Toroidal canonical momentum P_ϕ

  Ideal tokamak fields have perfect toroidal symmetry. Assuming this, the Hamiltonian describing a particle in an axisymmetric field is independent of the toroidal coordinate ϕ, which leads to the temporal invariance of the associated canonical momentum P_ϕ according to Noether's theorem [35].

$$P_\phi = mv_\phi R - eZ\psi_{pol} = const. \tag{2.24}$$

  where v_ϕ is the toroidal component of the velocity, Ψ is the flux surface and eZ is the ion charge. In a 2D magnetic equilibrium $\frac{dP_\phi}{dt} = 0$, however, if a symmetry breaking field is included, the conditions of Noether's theorem are

no longer fulfilled, leading to a temporal variation in P_ϕ. From equation 2.24 it can be extracted that a positive (negative) variation of P_ϕ forces the particle to drift to an inner (outer) flux surface Ψ, resulting into an inwards (outwards) transport of the orbit (see appendix A).

Adiabatic invariants:

In a less restrictive level than the constants of motion, we find the *adiabatic invariants*. This concept is relevant in physical systems where inhomogeneity of the fields is sufficiently *slow* compared to the characteristic periodic motions. In the adiabatic approximation the action integrals are not absolute constant, but the variation is sufficiently small to be considered invariant. Orbits in tokamaks have two main periodic motions: the gyromotion of the particle along the magnetic fields and the bouncing motion described by the gyrocentre in the poloidal plane, so two invariants associated to each motion are expected.

- First invariant: Magnetic moment

  The first adiabatic invariant is the magnetic moment and is related to the periodic gyromotion of a charged particle. Here, the canonical momentum $P_x = mv_xR_x$ is $P_\alpha = mv_\perp(\alpha)\rho(\alpha)$, as figure 2.2 shows. Calculating the associated action and considering the definition of μ used in 2.16:

  $$\oint mv_\perp(\alpha)\rho(\alpha)d\alpha = 2\pi mv_\perp\rho = \frac{4\pi m^2}{q}\mu = const. \tag{2.25}$$

  It is important to notice that the magnetic moment can only be considered as an adiabatic invariant in the approximation where $\nabla B/B \gg \rho$ and $\frac{dB/dt}{B} \ll \omega_c$.

- Second invariant: Longitudinal invariant

  The longitudinal invariant is associated to the bouncing motion of trapped particles between two turning points. A typical trapped particle is illustrated in figure 2.5. More details on the fast-ion orbit topology will be presented in section 2.5.

  The parallel velocity of the ion is integrated over a bouncing period:

$$J = \oint mv_{\parallel} dl \tag{2.26}$$

where l is the arc length described by the particle guiding centre along the field line. In this case, the guiding centre trajectory is not strictly closed, but if the $\nabla B/B \gg \rho$ condition is held and the time variation of the fields are small compared to the bouncing frequency, it can be regarded as approximately closed.

2.5 Orbit topology

As it was previously mentioned in this chapter, there is a wide variety of fast-ion present in a tokamak plasma including different energies, pitch and spatial distribution. The orbit topology of a particle is determined by its energy, pitch and the magnetic equilibrium. The different topologies can be included in two main categories: *trapped* and *passing* orbits.

2.5.1 Trapped orbits

Consider a charged particle in a nonuniform magnetic field. The conservation of the energy is implied as there are no external forces resulting into:

$$E = \frac{1}{2}mv_{\parallel}^2 + \frac{1}{m}mv_{\perp}^2 = \frac{1}{2}mv_{\parallel}^2 + \mu B = const. \tag{2.27}$$

where the μ definition 2.16 is included. Additionally, assuming the conditions necessary to consider that the magnetic moment is constant, when the particle explores a region where the magnetic fields is more intense, the parallel component of the velocity decreases to maintain E constant. In the limit case, the parallel velocity is zero and the movement of the particle is reversed in the parallel direction, leading to a confinement of the particle in the lower magnetic region. The position where $v_{\parallel} = 0$ is called turning point. This type of orbit is referred to as *trapped* particle and is illustrated in blue in figures 2.5 a) and b). Figure 2.5 a) illustrates the poloidal cross section of AUG vessel including a trapped particle in blue, showing that the motion is restricted to the low field side in the poloidal plane. However, this motion

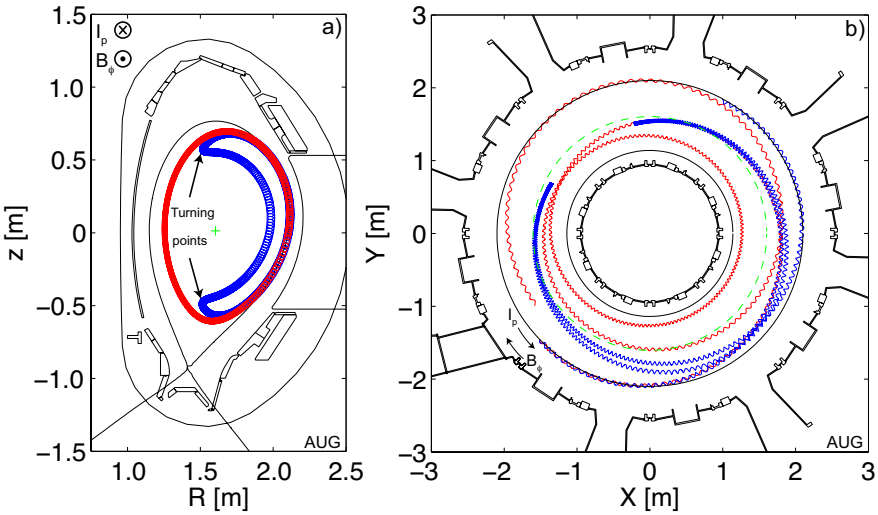

Figure 2.5: *a) Poloidal cross section of AUG showing a trapped (blue) and a passing (red) orbit. b) Toroidal cross section of AUG showing the toroidal projection of a trapped (blue) and a passing (red) orbit*

is not restricted in the toroidal direction as it is presented in figure 2.5 b), where the toroidal projection of the orbit shows the transit ϕ between two turning points.

The trapping in the poloidal plane only occurs if the maximum intensity of the magnetic field is such that:

$$B_{max}\mu \geq \frac{1}{2}mv_{\parallel}^2 + \mu B_{initial} \tag{2.28}$$

Introducing the definition of the pitch 2.1 and the invariance of μ, the expression can be rearranged into:

$$B_{max} \geq \frac{B_{initial}}{1-\Lambda^2} \tag{2.29}$$

2.5.2 Passing orbits

The magnetic field in a tokamak decreases as $1/R$, were R is the radial distance measured from the geometrical axis. If the maximum intensity of the magnetic field is not enough to reflect the parallel component of the particle, the orbit continues into the high field side circling the magnetic axis. These are called *passing* orbits. Figures 2.5 a) and b) illustrates the trajectory of a passing particle in red in the

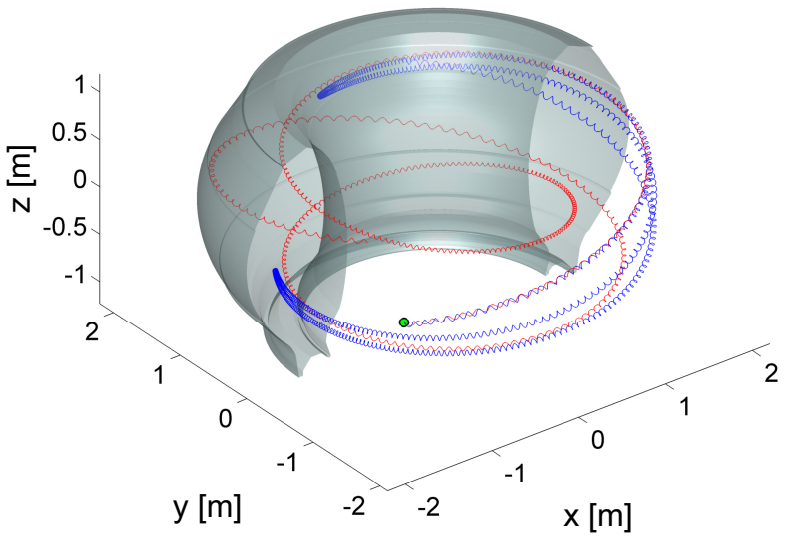

Figure 2.6: *3D representation of the AUG vessel including the orbits of a passing (red) and trapped (blue) ions calculated with the ASCOT code.*

poloidal and toroidal planes.

In the case of passing trajectories, the particle pitch never changes its sign and, consequently, the particle always moves in the same direction along the toroidal coordinate. Figure 2.6 shows a comparison of the 3D motion of a trapped and passing orbit.

2.6 Transport mechanisms in fusion plasmas

There are multiple ways to categorise particle transport depending on their nature and the underlying physical mechanisms. The classification presented here is one of the many possibilities that best fits the purposes of this work. Considering the transport mechanism, it can be divided into: classical, neoclassical and fluctuation induced transport.

- **Classical and Neoclassical transport model**

  The Classical transport theory provides a description to calculate transport coefficients of an ion species due to Coulomb collisions in the limit where the mean free path is short compared to the macroscopic scale length [36]. Under

this assumption, the transport occurs within local scales which allows one to neglect the geometry of the magnetic fields.

The Neoclassical theory extends the assumption of the short collisional free path to any arbitrary value [37, 38]. In this model, the transport has a dependence with the geometry of the magnetic field giving rise to different regimes depending on the collisionality. For high collisionality values where thermal particles are not able to complete an orbit before their trajectories are deflected by collisions is called the Pfirsh-Schlter [39]. The low collisionality limit, where the ions free path is long enough to complete an orbit, is referred to as the banana-plateau [40, 41].

Although the Neoclassical model has predicted successfully many features of thermal transport, this theory is limited by several aspects including the need of a minimum level of collisionality to ensure Maxwellian distributions or that the transport process remains Markovian. Moreover, this description is only applicable to static magnetic configurations.

- **Fluctuation induced transport**

  Transport due to electromagnetic fluctuations fall outside the scope of the neoclassical transport theory as it cannot ensure the Markovianity of the process or a static magnetic field. Although tokamaks provide excellent confinement of charged particles, the ideal axisymmetry of the magnetic fields can be broken by mechanical constraints of the machine, intrinsic plasma instabilities and the application of plasma control techniques [11, 42–46]. The interaction of charged particles with these 3D electromagnetic fields can lead to a particle transport and result into a degradation of the confinement [47]. These interactions are specially relevant in the case of fast-ions because of their long mean free paths which can lead to important displacement of their orbits with respect to the flux surfaces [18, 20–25, 48].

  – **Turbulent transport**

Fluctuations affecting the plasma profiles such as the electron density or temperature can lead to particle transport through turbulent mechanism [49, 50]. These fluctuations can be driven by free energy sources including mainly plasma gradients and currents and generate perturbations in the charge distribution [51]. One of the main contributions to the turbulent transport comes from the $E \times B$ component. In this case, the change in the charge distribution produces fluctuations in the electric potential originating an electric field $E = \nabla\phi$, which combined with the magnetic field B results in a velocity drift.

– **Wave-particle resonant transport**

Wave-particle interaction is widely accepted to be crucial in the description of particle transport, especially in low collisionality plasmas [47, 52, 53]. The resonant condition between a wave and a particle ensures that the interaction leads to a maximum variation of a given constant of motion, which occurs when the phase of a particle is similar to that of a wave. The changes in the particle constants of motion can lead to a redistribution of the particles in the phase-space.

In the theoretical framework provided in [54] for wave-particle resonant interactions, one can express a generic magnetic fluctuation in the form:

$$g(r, \phi, \theta) = \sum_{n,m} e^{i(n\phi + m\theta)} g_{n,m}(r) \tag{2.30}$$

using a set of coordinates (r, ϕ, θ) adequate to express the periodicity of the perturbation. Considering now the same fluctuation in the particle-moving frame, the periodicity of the particle motion can be used to describe the fluctuation as a function of the particle poloidal and toroidal precession frequencies as:

$$g(r, \phi, \theta) = \sum_{n,m,p} e^{i(n\bar{\omega}_d + p\omega_b)\tau} \tilde{g}_{n,m}(r) \tag{2.31}$$

introducing p as the harmonic associated to the poloidal transit. From equation 2.31 the resonant condition, obtained as the stationary of the wave-particle phase, reads:

$$\omega_0 = n\bar{\omega}_d + p\omega_b \tag{2.32}$$

for trapped particles, where ω_0 is the frequency of the mode. The synchronization resulting from this interaction causes continuous transport stands until the finite structures of the perturbation in the phase-space *detunes* the phase or until the topology os the orbit changes.

* **Overlapping**

  When one analyses the resonant conditions in a wave-particle system, it is likely to find several possible combinations of harmonics leading to different resonances. If these resonances are sufficiently close in the phase-space, it can lead to a where deterministic particle trajectories will move between two resonances in a chaotic manner. Chirikov criterion [55] is usually applied to determine the chaotic boundaries in the phase-space. This criterion is met when the width of two contiguos resonances is larger than the distance between them, leading to a chaotic region which causes particle transport.

Chapter 3

Nonlinear wave-particle resonances

In this chapter, previous results concerning the effects of the wave-particle interaction [52, 54, 56] are presented to provide the adequate framework for the nonlinear formulation. Using this results as the starting point, the formulation is expanded to derive an analytical expression for nonlinear resonant interactions that will be used to describe the fast-ion transport observed in both experimental (chapter 5) and numerical (chapter 6) results.

3.1 Unperturbed trajectories

To analyse the behaviour of a charged particle in the presence of a magnetic perturbation, the Hamiltonian can be written up to order ϵ_δ as [57]:

$$H = H_0 + \epsilon_\delta H_1 \tag{3.1}$$

with H_0 and H_1:

$$H_0 = \frac{1}{2} m v_\parallel^2 + \mu B \tag{3.2}$$

$$H_1 = -eZ v_\parallel A_\parallel \tag{3.3}$$

considering a purely magnetic perturbation. Introducing now a fluctuation in the parallel component of the magnetic potential with periodicites in the poloidal and

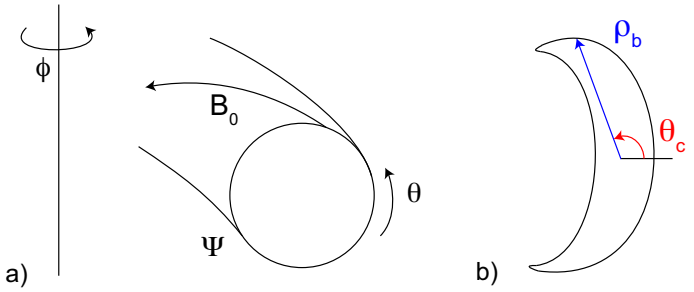

Figure 3.1: *a) Magnetic coordinates ($r(\Psi)$, θ, ϕ). b) Sketch of a banana orbit illustrating the coordinates (θ_c, ρ_b).*

toroidal angles θ, ϕ:

$$A_{\parallel} = \sum_{m,n} A_{\parallel n,m} \exp[i(n\phi + m\theta)] \tag{3.4}$$

the perturbed Hamiltonian reads:

$$H_1 = -eZv_{\parallel} \sum_{m,n} A_{\parallel n,m} \exp[i(n\phi + m\theta)] \tag{3.5}$$

with n, m the toroidal and poloidal mode numbers and $A_{\parallel n,m}$ the Fourier coefficients of the perturbed magnetic potential.

Although poloidal and toroidal angles θ and ϕ are adequate to exhibit the field periodicity (see figure 3.1 a)), the perturbation can be analysed in terms of the action angle variables, with angles (α_1, α_2, α_3) and associated actions (J_1, J_2, J_3) [58]. Here the magnetic momentum is assumed invariant, so there is no dependence on α_1. In the following, only trapped particles will be considered as they constitute the majority of the ion population at the plasma edge in the LFS, where the NBI deposition has a maximum. Considering this, the poloidal angle $\alpha_2 = \theta_c$, defined as the banana phase angle of the particle as shown in figure 3.1 b), and the toroidal drift $\alpha_3 = \xi$ are given by [59, 60]:

$$\theta = \tilde{\Theta}(\theta_c) \qquad \phi = \xi + q\tilde{\Theta}(\theta_c) + \tilde{\phi}(\xi) \tag{3.6}$$

where $\tilde{\Theta}$ and $\tilde{\phi}$ are periodic functions of θ_c and ξ. Considering this and neglecting $\tilde{\phi}(\xi)$, the new coordinates for deeply trapped particles read:

$$\theta = \theta_0 \sin\theta_c \qquad \phi = \xi + q\theta_0 \sin(\theta_c) \tag{3.7}$$

Although this calculation was made for deeply trapped particles, it can be performed for general periodic functions of $\tilde{\Theta}$ and $\tilde{\phi}$. Introducing now the particle bounce frequency (ω_b):

$$\omega_b = \frac{2\pi}{\oint d\theta/\dot{\theta}} \tag{3.8}$$

which can be related to θ_c as $\theta_c = \omega_b \tau$, where τ is a time variable that follows the particle location along the poloidal trajectory of period $2\pi/\omega_b$. Using the banana centre coordinates and associated frequencies, the parallel component of the velocity can be written as:

$$\left.\begin{aligned} \omega_b &= \frac{d\theta_c}{dt} \\ \frac{d\theta}{dt} &= \mathcal{J} v_\parallel \end{aligned}\right\} \longrightarrow d\theta_c = \omega_b \frac{d\theta}{\mathcal{J} v_\parallel} \rightarrow v_\parallel = \frac{\theta_0 \omega_b}{\mathcal{J}} \cos\theta_c = \frac{\theta_0 \omega_b}{2\mathcal{J}} e^{\pm i\theta_c} \tag{3.9}$$

with $\mathcal{J}$ the Jacobian of the transformation $\mathcal{J} = \mathbf{B} \cdot \nabla\theta / B$. Including equation (3.9) in the Hamiltonian (eq. (3.5)), this gives:

$$H_1 = -eZ \frac{\theta_0 \omega_b}{2\mathcal{J}} \sum_{n,m} A_{\parallel n,m} \exp[\pm i\theta_c] \exp[i(m\theta + n\phi)] \tag{3.10}$$

which can be rewritten using equations (3.7) as a function of θ_c, ξ as:

$$H_1 = -eZ \frac{\theta_0 \omega_b}{2\mathcal{J}} \sum_{n,m} A_{\parallel n,m} \exp[\pm i\theta_c] \exp[i(m + nq)\theta_0 \sin\theta_c] \exp[in\xi] \tag{3.11}$$

Using the Jacobi-Anger identity [61], the term $\exp[i(m+nq)\theta_0 \sin\theta_c]$ in expression (3.11) can be written as its Fourier expansion in the harmonics associated to θ_c:

$$\exp[i(m + nq)\theta_0 \sin\theta_c] = \sum_p J_p \exp[ip\theta_c] \tag{3.12}$$

with p the bounce harmonic and J_p a Bessel function of $(m + nq)\theta_0$. Therefore,

the hamiltonian reads:

$$H_1 = -eZ\frac{\theta_0\omega_b}{2\mathcal{J}}\sum_{n,m,p} A_{\parallel n,m}J_p \exp[\pm i\theta_c]\exp[ip\theta_c]\exp[in\xi] \tag{3.13}$$

Using the canonical equations of Hamilton, the time evolution of P_ϕ can be obtained from:

$$\frac{dJ_3}{dt} = -\frac{\partial H}{\partial \alpha_3} \rightarrow \frac{dP_\phi}{dt} = -\frac{\partial H}{\partial \xi} \tag{3.14}$$

Combining equations (3.13) and (3.14):

$$\frac{dP_\phi}{dt} = eZ\frac{\theta_0\omega_b}{2\mathcal{J}}\sum_{n,m,p} inA_{\parallel n,m}J_p \exp[i(n\xi + (p\pm 1)\theta_c)] \tag{3.15}$$

which can be expressed as a function of the particle frequencies (ω_b, $\bar{\omega}_d$) associated to the coordinates θ_c, ξ in the form:

$$\frac{dP_\phi}{dt} = eZ\frac{\theta_0\omega_b}{2\mathcal{J}}\sum_{n,m,p} inA_{\parallel n,m}J_p \exp[i(n\bar{\omega}_d + p\omega_b)\tau] \tag{3.16}$$

where the bounce harmonic $p\pm 1$ was renamed to p without any loss of generality.

In the theoretical framework of fast-ion transport, it is important to define the conditions for which resonant transport can happen as a consequence of the interaction between a plasma ion and waves. The resonant condition for trapped ions provided by the stationarity of the wave-particle phase in equation (3.16) (i.e. $\frac{d}{dt}(n\bar{\omega}_d + p\omega_b)\tau = 0$) can be written as:

$$\omega_0 - n\bar{\omega_d} - p\omega_b = 0 \tag{3.17}$$

This expression holds for the unperturbed orbits where ω_0 is the frequency of the perturbation, providing the resonant condition for the linear case. In order to include nonlinear effects in the resonant condition, it is necessary to include the changes in the particle trajectories due to the perturbed fields in the Hamiltonian.

3.2 Perturbed trajectories

If a linear resonant condition is not satisfied, it is assumed that the dominant impact of the perturbation is to modulate periodically the bounce-averaged particle displacement [52], introducing a shift in the particle trajectory accumulated through each τ period. The expressions used to describe this motion containing the correction added to the trajectories are given by:

$$\theta = \tilde{\Theta}(\theta_c) + \Delta\theta \tag{3.18}$$

$$\phi = \xi + q\tilde{\Theta}(\theta_c) + \Delta\phi \tag{3.19}$$

with

$$\Delta\theta = \int_0^\tau \delta\theta dt = \int_0^\tau \delta\dot{\theta}\frac{d\theta}{\dot{\theta}} \tag{3.20}$$

$$\Delta\phi = \int_0^\tau \delta\dot{\phi}\frac{d\theta}{\dot{\theta}} \tag{3.21}$$

the corrections to θ and ϕ due to the finite amplitude of the perturbation accumulated over a bounce period τ.

Using these expressions for θ and ϕ, the Hamiltonian in (3.5) reads:

$$H_1 = -eZ\frac{\theta_0\omega_b}{2\mathcal{J}}\sum_{n,m} A_{\|n,m}J_p \exp[\pm i\theta_c]\exp[ip\theta_c]\exp[in\xi]\exp[i(m\Delta\theta + n\Delta\phi)] \tag{3.22}$$

Considering $\Delta\theta$ and $\Delta\phi$ periodic functions of θ_c and ξ with periods $2\pi/\omega_b$, $2\pi/\bar{\omega}_d$:

$$\exp[i(m\Delta\theta + n\Delta\phi)] = \exp[i\Xi_{n,m}(p\theta_c + n\xi)] = \sum_l S_{n,m,l}\exp[il(p\theta_c + n\xi)] \tag{3.23}$$

with $\Xi_{n,m}$ a periodic function in $(p\theta_c + n\xi)$. Including equation (3.23) in (3.22):

$$H_1 = -eZ\frac{\theta_0\omega_b}{2\mathcal{J}}\sum_{n,m,p,l} A_{\|n,m}J_p \exp[\pm i\theta_c]\exp[ip\theta_c]\exp[in\xi]\exp[il(p\theta_c + n\xi)] \quad (3.24)$$

which can be readily arranged as:

$$H_1 = -eZ\frac{\theta_0\omega_b}{2\mathcal{J}}\sum_{n,m,p,l} A_{\|n,m}J_p \exp[i(p \pm 1 + lp)\theta_c) + i(1+l)n\xi] \quad (3.25)$$

Using equation (3.14), the temporal evolution of P_ϕ is:

$$\begin{aligned}\frac{dP_\phi}{dt} &= -eZ\frac{\theta_0\omega_b}{2\mathcal{J}}\sum_{n,m,p,l} A_{\|n,m}J_p in(1+l)\exp[i(p \pm 1 + lp)\theta_c) + i(1+l)n\xi] \\ &= -eZ\frac{\theta_0\omega_b}{2\mathcal{J}}\sum_{n,m,p,l} A_{\|n,m}J_p in(1+l)\exp[i(p \pm 1 + lp)\omega_b)\tau + i(1+l)n\bar{\omega}_d\tau]\end{aligned}$$

Therefore, the resonant condition for stationary perturbations ($\omega_0 = 0$) can be expressed as:

$$\frac{\omega_b}{\bar{\omega}_d} = \frac{n(l+1)}{p(l+1) \pm 1} \quad (3.26)$$

This expression provides the ratio between bouncing and toroidal particle frequencies that must be met to produce a resonant interaction between ions and the magnetic perturbation caused by the RMP fields. In chapter 6 this equation is used to analyse and identify the relevant resonances leading to fast-ion transport for different magnetic perturbations as a function of n, l and p.

Chapter 4

Methodology

4.1 Experimental Setup

This section gives an overview of the main elements involved in the set up of the experiments that will be analysed throughout this work. As a part of the set up, a description of the ASDEX Upgrade tokamak including the RMP coil system installed in AUG to generate the 3D perturbations is presented. The characteristics of the Neutral Beam Injector as the main fast-ion source will be introduced.

4.2 ASDEX Upgrade tokamak

ASDEX Upgrade [62] is a medium-size divertor tokamak located at the Max-Planck Institute for Plasma Physics in Garching (Germany). In the AUG, the axisymmetric magnetic field is generated by a set of 16 copper coils wrapped around the vessel and arranged evenly spaced along the toroidal direction. Additionally there are 17 coils used for the divertor, the plasma current and to control the position and shape of the plasma. Table 4.1 presents the main AUG parameters.

4.2.1 Resonant Magnetic Perturbations

As it was mentioned in chapter 2, plasma instabilities, in particular, ELMs can lead to a large enhancement of the radial transport. By applying a controlled magnetic

Total height	9 m
Major radius	1.6 m
Minor radii	0.5/0.8 m
Magnetic field	3.9 T
Plasma current	up to 1.4 MA
Plasma heating (NBI)	20 MW
Plasma heating (ICRH)	6 MW
Plasma heating (ECRH)	4 MW
Plasma mixture	Hydrogen, deuterium
Plasma temperature	4 keV
Plasma density	up to $2 \cdot 10^{20}$ m^{-3}
Vessel material	Tungsten

Table 4.1: *Main AUG parameters.*

perturbation, we can degrade the edge confinement enough to lower the pressure gradient such that the peeling-balloning boundary for Type-I ELMs is not hit. In order to mitigate ELMs by means of magnetic perturbations, AUG has 16 coils installed in two rows, one above the midplane and one below, which generate Magnetic Perturbations (MP) [11, 63]. Figure 4.1 shows the distribution of the RMP coils in AUG and the generated magnetic perturbation along the separatrix.

Axisymmetric fields have nested flux surfaces, which ensure that the particle transport is mostly produced in the direction of the field lines. However, when a magnetic perturbation is applied, the field lines can be distorted, creating magnetic islands on the resonant surfaces $q = m/n$, with m and n the poloidal and toroidal mode numbers respectively. Figure 4.2 shows the Poincaré plots corresponding to an axisymmetric magnetic field and a 3D perturbative field generated by a $n = 2$ coil configuration, where the island chains appear at the resonant surfaces $q = 3/2, 2, 5/2, 3, 7/2$. If the resonant surfaces are too close or the amplitude of the island is large enough, an overlapping of two or more island chains can lead to a chaotic region. In figure 4.2 b) the region close to the separatrix ($\rho_{pol} \approx 1$), where the amplitude of the perturbation is larger, field line chaos can be observed.

The coil set up in AUG allows $n = 1, 2, 4$ toroidal symmetries depending on the applied current. Figure 4.3 shows the intensity of the current flowing through each coil (figure 4.3 a)) and the radial component of the associated $n = 2$ magnetic field

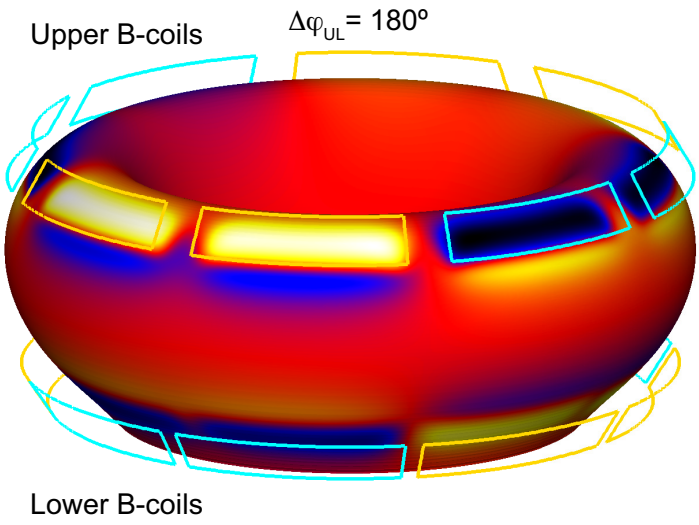

Figure 4.1: *a) Schematics of RMP coils set up in AUG with associated perturbative magnetic field for* $\Delta\varphi_{UL} = 180°$.

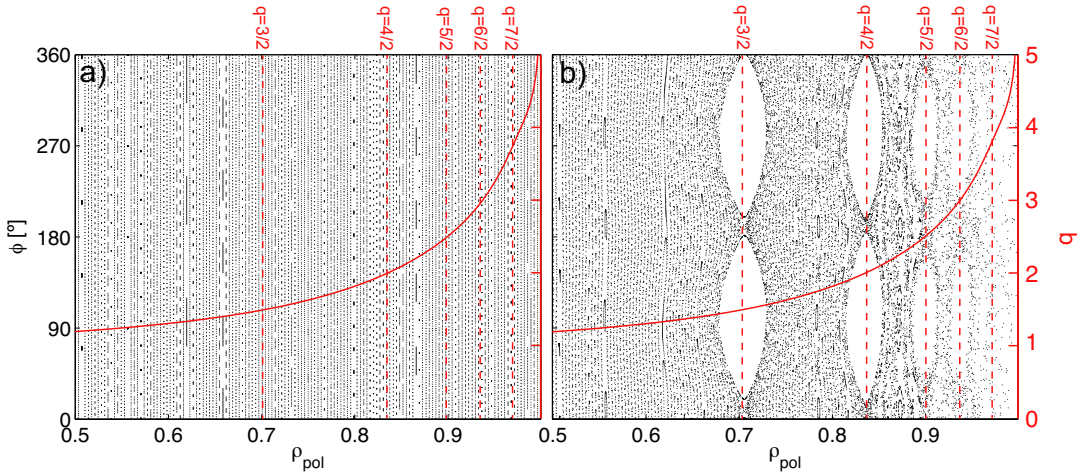

Figure 4.2: *Toroidal Poincaré maps of the magnetic fields for: a) axisymmetric field and b) perturbed field calculated with ASCOT. The q-profile of the magnetic field is shown in red together with the resonant magnetic surfaces.*

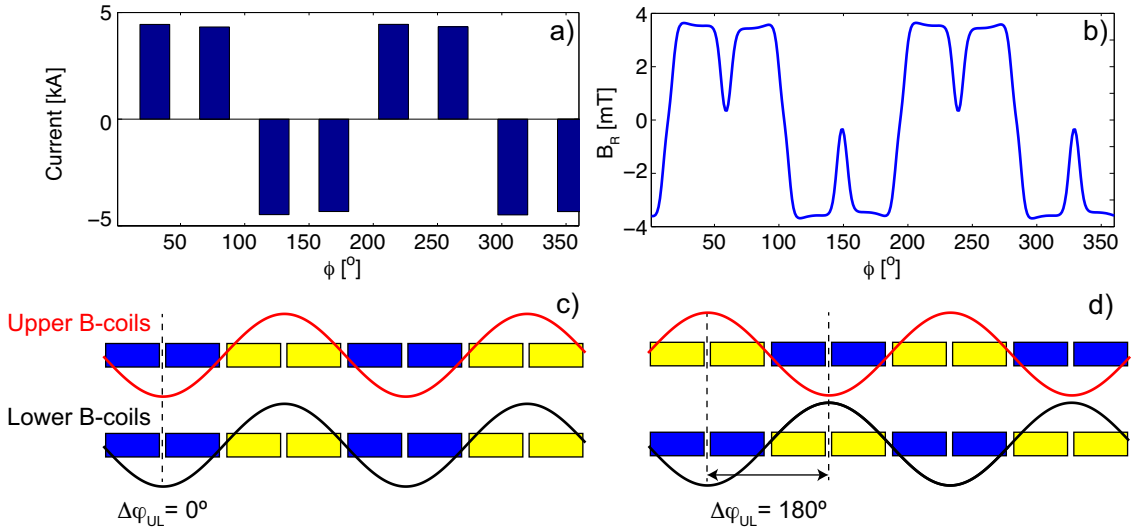

Figure 4.3: *a) Coil currents as a function of the toroidal location of the RMP coils. b) Radial component of the perturbative fields generated by the RMP coils. Phase shift between the upper and lower set of coils for: c)* $\Delta\varphi_{UL} = 0°$ *and d)* $\Delta\varphi_{UL} = 180°$ *configurations.*

(figure 4.3 b)). In addition to controlling the amplitude and toroidal symmetry of the perturbative fields, it is also possible to modify the phase shift between the upper and lower current sinusoids. Given the distribution of the coils along two rows at different z locations, by fixing one row and rotating the other the applied field can be *twisted*.

Figure 4.3 c) shows a typical $n = 2$ configuration in which the current values are the same for the upper and lower row. In this case, the phase shift between both sets is $\Delta\varphi_{UL} = 0°$. In figure 4.3 d), the upper coils currents are rotated so the phase between both signals is $\Delta\varphi_{UL} = 180°$. A change in the phase shift implies a modification of the poloidal mode spectra of the perturbation, which has an important impact on the distortion of the magnetic flux surfaces and particle confinement.

4.2.2 Neutral Beam Injector

The mechanism by which particles are accelerated and injected into the plasma as neutrals is described in section 2. In this section, the technical aspects of the NBI heating system at AUG is described.

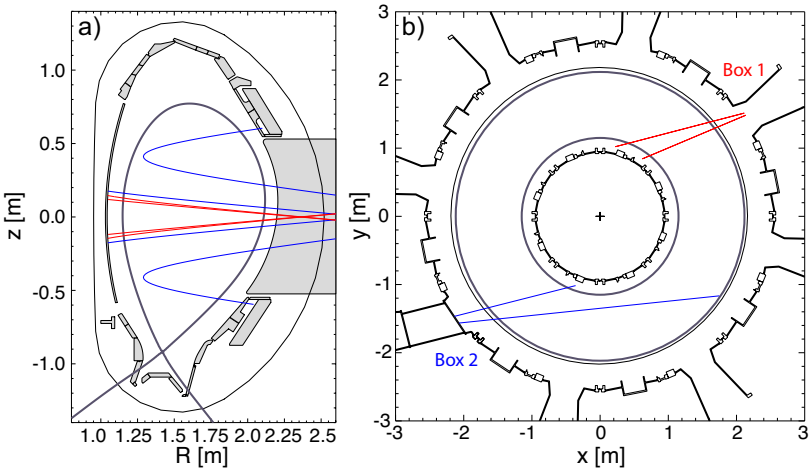

Figure 4.4: *Poloidal and toroidal sketches of the 8 neutral beam injectors installed in AUG.*

The NBI set up consists of two boxes at different toroidal locations, each one containing four beams capable of injecting a power of 2.5 MW per beam. The injection geometry of the 8 beams is shown in figure 4.4, in a poloidal (4.4 a)) and toroidal (4.4 b)) cross section of the vessel. One of the main features associated to each beamline is the fixed pitch value, conditioning the topology of the ionised particles. For injections parallel to the magnetic field lines, the dominant topology is passing, while the more radial injections generate a population of trapped particles. In figure 4.5, the birth distributions generated by different injectors are presented as a 2D histogram in the poloidal projection.

The NBI distribution decays exponentially with the path length as $I(x) = I_0 e^{-\nu x}$, where I_0 is the initial intensity, ν is the ionisation frequency and x is the distance travelled through the plasma. The beam distributions shown in figure 4.5, calculated with the BBNBI tool [64], show the exponential decay from the plasma edge, where most of the ionisations occur. However, as the vacuum is not perfect between the separatrix and the vessel, we can find a small population of fast-ions outside the separatrix. To illustrate this, figure 4.6 shows the radial profile of the NBI distribution for radial (NBI#2) and tangential (NBI#6) injections. This small population of fast-ions at the edge is extremely susceptible of being affected by the radial trans-

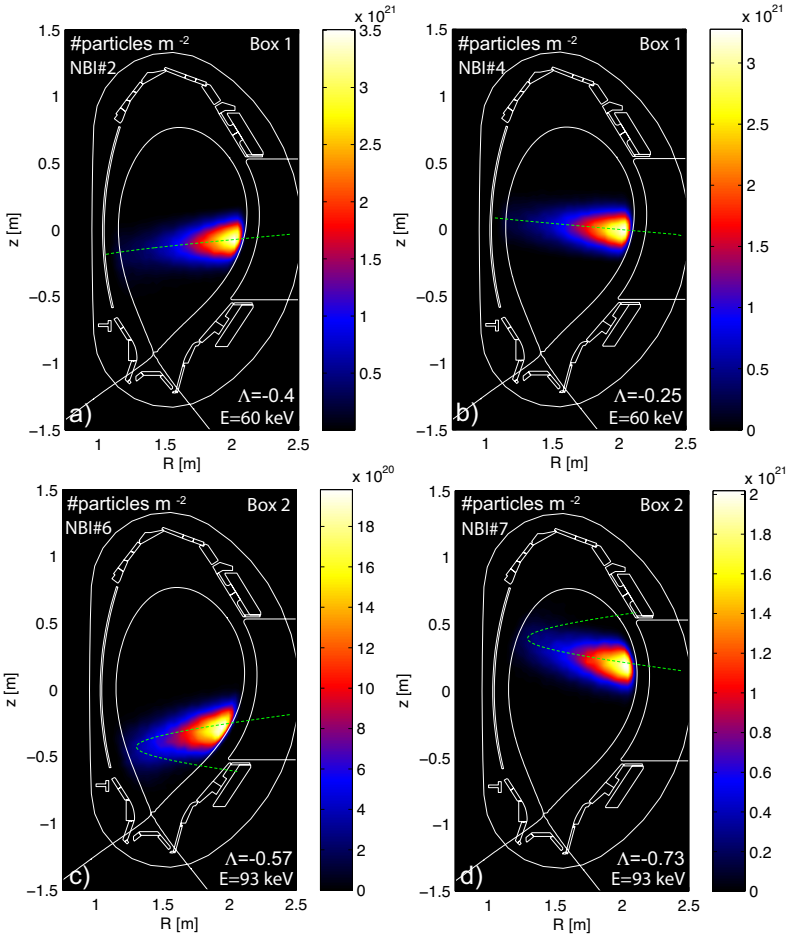

Figure 4.5: *2D histograms showing the poloidal cross section of the NBI brith distribution corresponding to: a), b) radial injections from box 1 and c), d) tangential injections from box 2.*

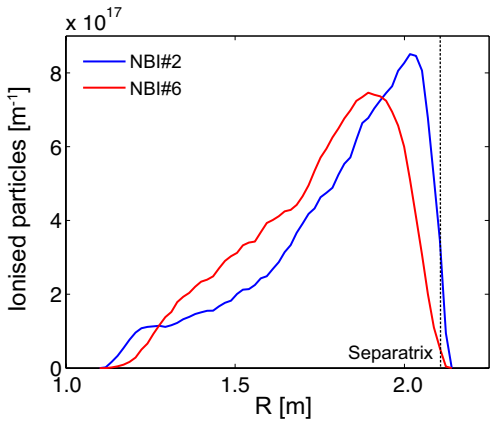

Figure 4.6: *Radial histogram showing the NBI birth distribution of: a) radial injection and b) tangential injection.*

port induced by magnetic perturbation as the field lines in this region bring those particles very close to the RMP coils.

4.3 Numerical tool: The ASCOT code

The ASCOT code [26] is a numerical simulation tool used to follow the trajectories of minority particle species, including Coulomb interactions with the bulk plasma through a Monte Carlo operator [65]. In simulations of fusion plasmas, large statistics are required to produce accurate results. This problem is handled in ASCOT by means of considering the minority distribution as a particle ensemble that follows the Fokker-Planck equation [66]:

$$\frac{\partial f}{\partial t} + \dot{x} \cdot \frac{\partial f}{\partial x} = \left(\frac{\partial f}{\partial t}\right)_{collisions} \tag{4.1}$$

where $f(\mathbf{x})$ is the particle distribution in the phase space $\mathbf{x} = (\mathbf{r}, \mathbf{v})$ and $\left(\frac{\partial f}{\partial t}\right)_{collisions}$ is a stochastic Monte Carlo operator which models the effect of the Coulomb interactions as small changes in the particle velocity. Although test particles in ASCOT are affected by the collisions with the bulk plasma, the interaction between the same species or the effect of a fast-ion distribution on the plasma is not considered.

4.3.1 Particle tracing

Full orbit trajectories in ASCOT are calculated using the noncanonical Hamiltonian equations of motion derived in section 2.2:

$$\dot{\mathbf{v}} = \frac{e}{m}(\mathbf{E} + \mathbf{v} \times \mathbf{B})$$
$$\dot{\mathbf{r}} = \mathbf{v}$$

for a particle of charge e, mass m and velocity $\mathbf{v}$. This system constitutes a set of 6 equations in the particle velocity space which can be solved in ASCOT using leap-frog and fourth-order Runge-Kutta [67] integrating methods. However, considering that the Runge-Kutta algorithm can lead to numerical drifts causing a variation in the total energy, the leap-frog is introduced to trace the particle position and velocity as:

$$\mathbf{v}_{i+1} = \mathbf{v}_i + \frac{e}{m}\left(\mathbf{E}_i + \frac{\mathbf{v}_{i+1} + \mathbf{v}_i}{2} \times \mathbf{B}_i\right)\Delta t \tag{4.2}$$

$$\mathbf{r}_{i+1} = \mathbf{r}_i + \mathbf{v}_i \Delta t \tag{4.3}$$

This method ensures the conservation of the total particle energy [68] through $\mathbf{v}_{i+1}^2 = \mathbf{v}_i^2$ in the $\mathbf{E} = 0$ case.

If a magnetic field is slowly varying in the time and space scales compared to the particle motion, i.e. the spatial length of the field is bigger than the particle gyroradii $\nabla B/B \gg \rho$ and the frequency relative to the local field is small compared to the gyrofrequency $\frac{dB/dt}{B} \ll \omega_c$, the guiding centre approach is valid and it is accurate to use the equations described in section 2.2. Aiming to reduce the simulation time, the guiding centre approach was introduced by ignoring the gyromotion of the particle, describing only the motion of the gyrocentre. To illustrate the different descriptions, figure 4.7 shows the trajectory of a trapped ion in full orbit and guiding centre approach. The use of this approach reduces significantly the cpu-time of a simulation, however, this description requires the conservation of the particle magnetic momen-

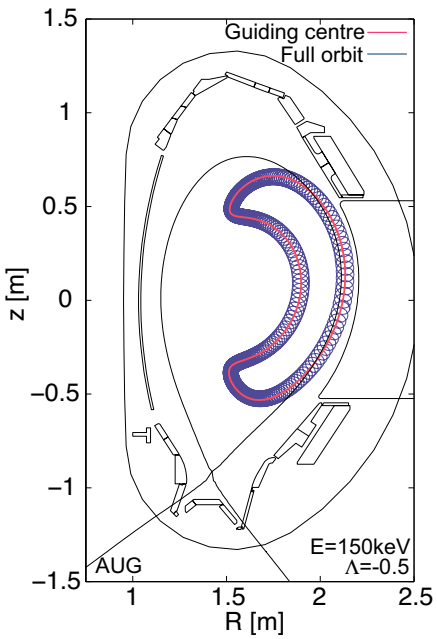

Figure 4.7: *Trajectory of a trapped particle integrated in full orbit motion (blue) and using the guiding centre approach (red).*

tum.

In this work, the magnetic fields involved are static so the second condition is automatically satisfied, but the radial field structures are comparable to the particle gyroradius. In this case a full orbit description must be kept to maintain the accuracy of the simulations. This matter will be further discussed in section 6.

4.3.2 ASCOT inputs

The ASCOT simulations require a set of inputs that offer the possibility to provide a given run with an accurate and realistic scenario. The main inputs are magnetic background, particle inputs, plasma kinetic profiles and wall geometry.

Particle input

The initial particle distribution must contain the 6 velocity space coordinates $(\mathbf{r}, \mathbf{v})$ to be traced in full orbit motion or 5 coordinates $(\mathbf{R}, \Lambda, E)$ in the guiding centre

approach. The ASCOT code has an independent tool called BBNBI [64] capable of generating the fast-ion distribution produced by the NBI injectors, which has been benchmarked with other neutral beam ionisation models such as PENCIL [69] or NUBEAM [70]. BBNBI has been developed to include the beam geometries of the most relevant current tokamaks such as AUG, ITER, DIII-D and MAST. In this work, all the NBI birth distributions were generated using this tool.

Magnetic background

In order to trace the charged particles, a model of the magnetic background is needed. This includes the 3 components of the magnetic field (B_R, B_z, B_ϕ) in cylindrical coordinates arranged in a matrix that can be either 2D or 3D. For the axisymmetric case, ASCOT calculates the magnetic field components from the B_ϕ and poloidal flux Ψ provided by any equilibrium reconstruction code. For 3D magnetic fields, ASCOT extracts the (B'_R, B'_z, B'_ϕ) perturbative components and combines them with the axisymmetric field.

Plasma kinetics

To ensure the accuracy of the Coulomb collision operator, ASCOT needs to be provided with the plasma kinetic profiles, which includes the density and temperature of ions and electrons as a 1D profile dependent of the radial coordinate ρ_{pol}. These profiles are not only important for the Coulomb collision operator, but also for the NBI ionisation profile generated with BBNBI. Additionally, it is possible to include the plasma rotation velocity and the radial electric field.

Wall geometry

Simulating particle losses requires a limiting area for the calculation set by the vessel walls. ASCOT works with both 2D and 3D realistic wall geometries. For the 2D case, only a poloidal cross-section of the vessel is needed. As 3D elements of the plasma facing components can be of important to accurately determine the wall heat loads caused by escaping ions, it is possible to provide ASCOT with a triangular mesh to model the 3D details of the wall. Equally important is the determination of a

particle intersection with the walls. In ASCOT, the method used to identify particle collisions with wall elements is a ray-polygon collision detector algorithm [71], which calculates the intersection between a line and a planar element.

Coulomb interactions

The interaction of energetic particles with the bulk plasma through Coulomb collisions is modeled in ASCOT by means of a Monte Carlo operator that evaluates the interactions between time steps. The collision operator in the particle phase space introduces a variation in the particle velocity [26] which contains a deterministic term together with a stochastic part. The deterministic term includes the Hamilton equation and a collision friction term depending on the collision frequency which brings the particle energy towards the energy thermal value. The second term introduces stochastic processes that widens the velocity distribution.

Chapter 5

Experimental Results

Several experiments have been carried out at AUG to show the impact of the RMPs poloidal mode spectra on ELM mitigation and associated fast-ion losses. In this chapter, the results of experiment AUG#33143 is presented.

The discharge AUG#33143 was carried out in an ELMy H-mode, with a safety factor value of $q_{95} = 3.8$ at 95% of the poloidal flux surface, low electron collisionality $\nu_e^* = 0.2$ and high normalised $\beta_N = 2.4$ [72]. The source of energetic particles was introduced by means of 5 MW NBI distributed on 2 sources with 2.5 MW from 2 NBI boxes, one at 60 kV (NBI#3) and the other at 93 kV (NBI#8). Figure 5.2 shows the corss-section of AUG including the plasma shape and active beams.

In this experiment, a perturbation with a toroidal symmetry number $n = 2$ was generated by the RMP coils. The current at the lower coils was fixed, while the current on the upper coils was rotating at 2 Hz, introducing a phase shift ($\Delta\varphi_{UL}$) that resulted in a continuous scan of the poloidal mode spectra. In figure 5.1 a) the coil currents corresponding to 3 different coils are presented as a function of time, showing one of the lower currents (red), which is kept constant, and two of the upper (black and blue) currents that were changing continuously. Although the main toroidal mode number is $n = 2$, the symmetry is limited by the finite number of coils, which introduces additional weak sidebands. Figures 5.1 b) and c) show the radial component of the perturbation including all harmonics resulting from the

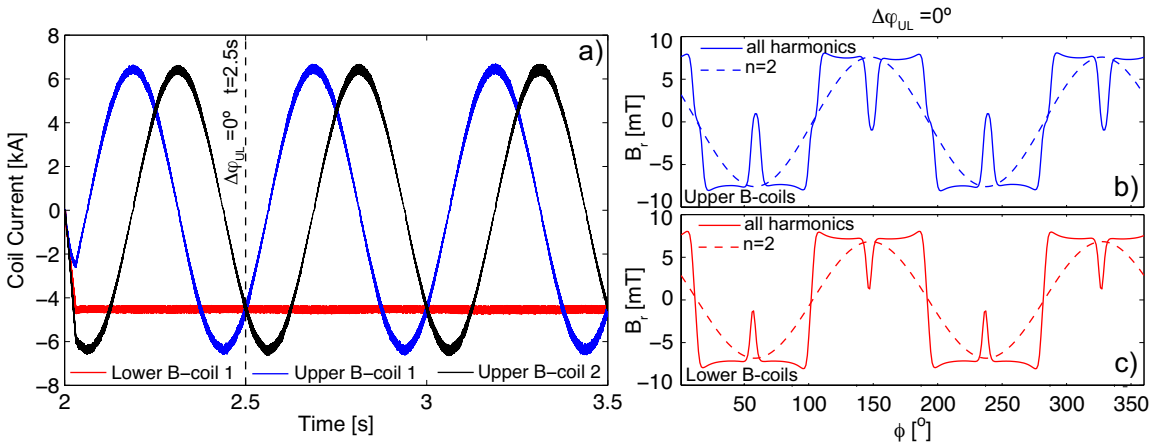

Figure 5.1: *a) RMP currents as a function of time for one coil of the lower row (red) and two coils of the upper row (black and blue). Radial component of the perturbative field corresponding to: b) upper coil row including all toroidal harmonics (solid blue) and only $n = 2$ harmonic (dashed blue), and c) lower coil row including all toroidal harmonics (solid red) and only $n = 2$ harmonic (dashed red).*

calculation of the magnetic fields using Biot-Savart law compared to the pure $n = 2$ toroidal component.

Figure 5.3 shows the time evolution of several plasma parameters corresponding to shot #33143. The fast-ion losses were measured by the Fast Ion Lost Detector (FILD) system [73]. In particular, the escaping ions measured with the FILD at the midplane ($z = 0.3\,m$) and toroidal location $\phi = 123.5°$ (FILD2) are presented in figure 5.3 a). Figure 5.3 b) shows the time traces of the electron density at the plasma edge and core. The poloidal currents at the outer divertor obtained from shunt measurements (figure 5.3 c)) are typically used in AUG to detect ELM instabilities.

The RMP coils in AUG are installed close to the Passive Stabilisation Loop (PSL)[74], where the induced image currents can attenuate the rotating perturbative fields. In this experiment the rotating fields had a frequency of 2 Hz, which required a correction by the PSL in order to determine the accurate value of $\Delta\varphi_{UL}$. Figure 5.3 d) shows the temporal dependence of the poloidal mode spectra $\Delta\varphi_{UL}$ including the delay induced by the PSL (blue) and the curve without the correction as reference (green).

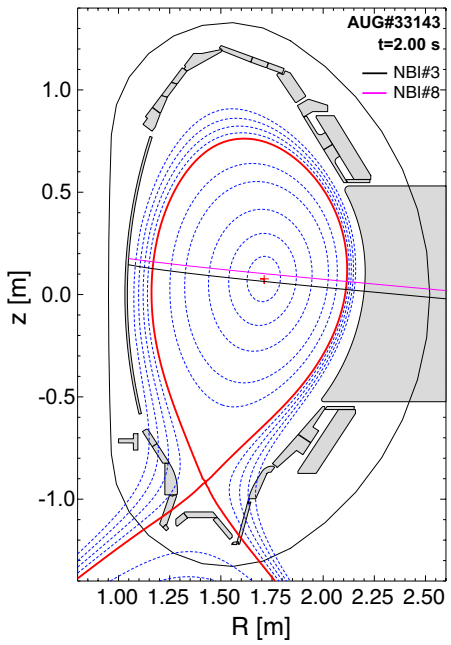

Figure 5.2: *Poloidal cross-section of AUG#33143 equilibrium at t=2.00 s showing the separatrix (red), constant flux surfaces (blue), and the beamline of injectors NBI#3 (black) and NBI#8 (magenta).*

When the RMP coils are turned on at t=2 s, figures 5.3 a)-c) show density pump out, partial ELM mitigation and fast-ion losses. A modulation can also be observed as the response is different for different values of $\Delta\varphi_{UL}$. These effect is especially evident in the FILD signal, where fast-ion losses only appear for certain coil configurations between $\Delta\varphi_{UL} = 100° - 200°$.

This experiment reveals that $\Delta\varphi_{UL}$ has a strong effect on the plasma parameters, suggesting that particle transport caused by the symmetry-breaking fields can be modified by the poloidal mode spectra. In the following chapters, an analysis of the fast-ion confinement in the presence of 3D perturbative fields is presented to provide an explanation of the underlying physical transport mechanism by means of numerical simulations and an analytical model.

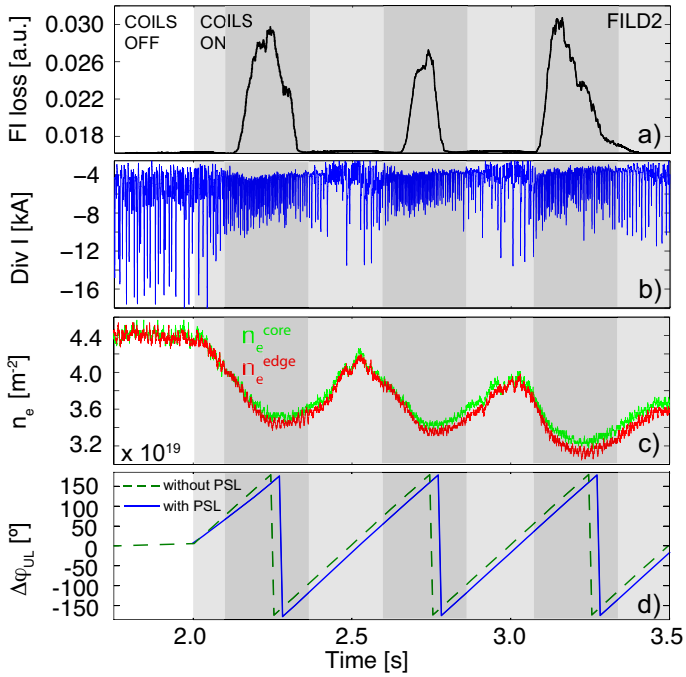

Figure 5.3: *AUG#33143. a) Fast-ion losses temporal signal measured by FILD detector. b) Temporal evolution of the outer divertor current shunt measures. c) Time traces of edge and core electron line integrated density. d) Poloidal mode spectra of the RMP perturbative fields as a function of time with (blue) and without (dashed green) the PSL correction.*

Chapter 6

Numerical results

In this chapter the results of the fast-ion simulations carried out with the ASCOT code to asses the ion transport in the presence of RMP with different poloidal mode spectra are presented. This chapter is structured as follows: first a description of the inputs used in these simulations is provided, then a comparison of the simulated fast-ion losses and the AUG experiment described in chapter 5 is shown and finally the *Edge Resonant Transport Layer* is introduced as the region where increased transport of trapped particles is identified, with the resulting particle losses caused by a resonant interaction with externally applied magnetic perturbations.

6.1 Input Modelling

The viability of this numerical model is based on its capability of reproducing the measured data. For this purpose, the particle input and magnetic background were carefully calculated from experimental data to simulate the fast-ion loss behaviour in an environment as similar as possible to the experiment at conditions of the discharge AUG#33143.

6.1.1 Input particles

The birth profile corresponding to NBI#8 was calculated with the BBNBI [64] module using the measured density and temperature plasma profiles shown in figures 6.1 a) and b). As was presented in chapter 5, when the magnetic perturbation was

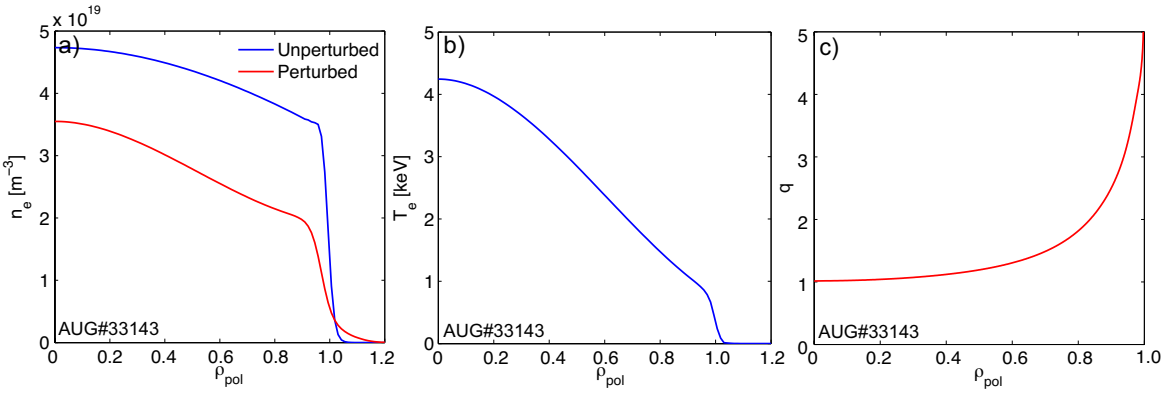

Figure 6.1: *Profiles of: a) Electron density for the perturbed (red) and unperturbed (blue) case, b) Unperturbed electron temperature profile as a function of ρ_{pol} and c) Safety factor profile as a function of ρ_{pol}*

applied in experiment AUG#33143, the density profile decreased and also presented a modulation with the perturbed poloidal mode spectra. The variation of the density profile can cause differences on the NBI birth profile, which in turn, can affect the fast-ion losses especially at the scrape-off layer (SOL). For these simulations, the unperturbed density and temperature profiles (figure 6.1) are kept constant to isolate the effect of the poloidal mode spectra on the losses. The resulting initial distribution of the NBI#8 ions is shown in figure 6.2 as the fast-ion surface density projected onto the poloidal and toroidal cross-sections.

6.1.2 Magnetic background

The magnetic input was generated as a combination of the axisymmetric field and the 3D perturbative fields. For these simulations, the AUG axisymmetric equilibrium was provided by the CLISTE code [75] using the values of the poloidal field currents and the toroidal magnetic field. The radial profile of the safety factor for the analysed discharge is shown in figure 6.1 c). The perturbed fields, including the plasma response, have been calculated with the MARS-F code [76], which is a single fluid, full MHD eigenvalue code in full toroidal geometry. These perturbative fields include the main harmonic perturbation $n = 2$ as well as the secondary harmonic $n = 6$ given by the realistic geometry of the MP coils. As a result, the values of the combined fields are obtained in a cylindrical grid which is interpolated in ASCOT

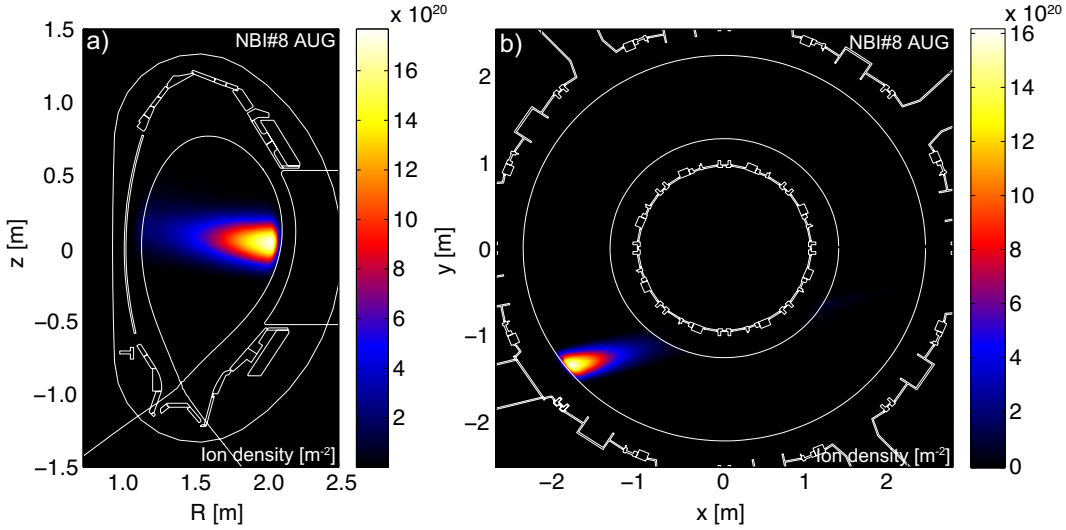

Figure 6.2: *2D histogram showing the surface density of the initial NBI#8 ion distribution projected onto the: a) poloidal and b) toroidal cross section.*

using cubic splines.

In order to validate the simulations against the experiment, the 3D fields were calculated for different time points scanning the entire poloidal mode spectra of the perturbation. Figure 6.3 presents the toroidal and poloidal Poincaré maps of the magnetic field lines of the RMP perturbation for coil configuration $\Delta\varphi_{UL} = 40°$ in vacuum approach and configurations $\Delta\varphi_{UL} = 40°$ and $\Delta\varphi_{UL} = 260°$ including the plasma response showing the magnetic island chains at ρ_{pol}=0.7-1.0.
To illustrate the impact of the poloidal spectrum on the poloidal structures of the 3D fields, figure 6.4 shows the radial component of the perturbation (δB_R) in a poloidal cross section of the AUG vessel at a toroidal angle $\phi = 0°$ for two different coil configurations. In this configuration, the lower coils are fixed and the upper coils are rotating to modify the poloidal spectra, also changing the structure and intensity of the plasma response.

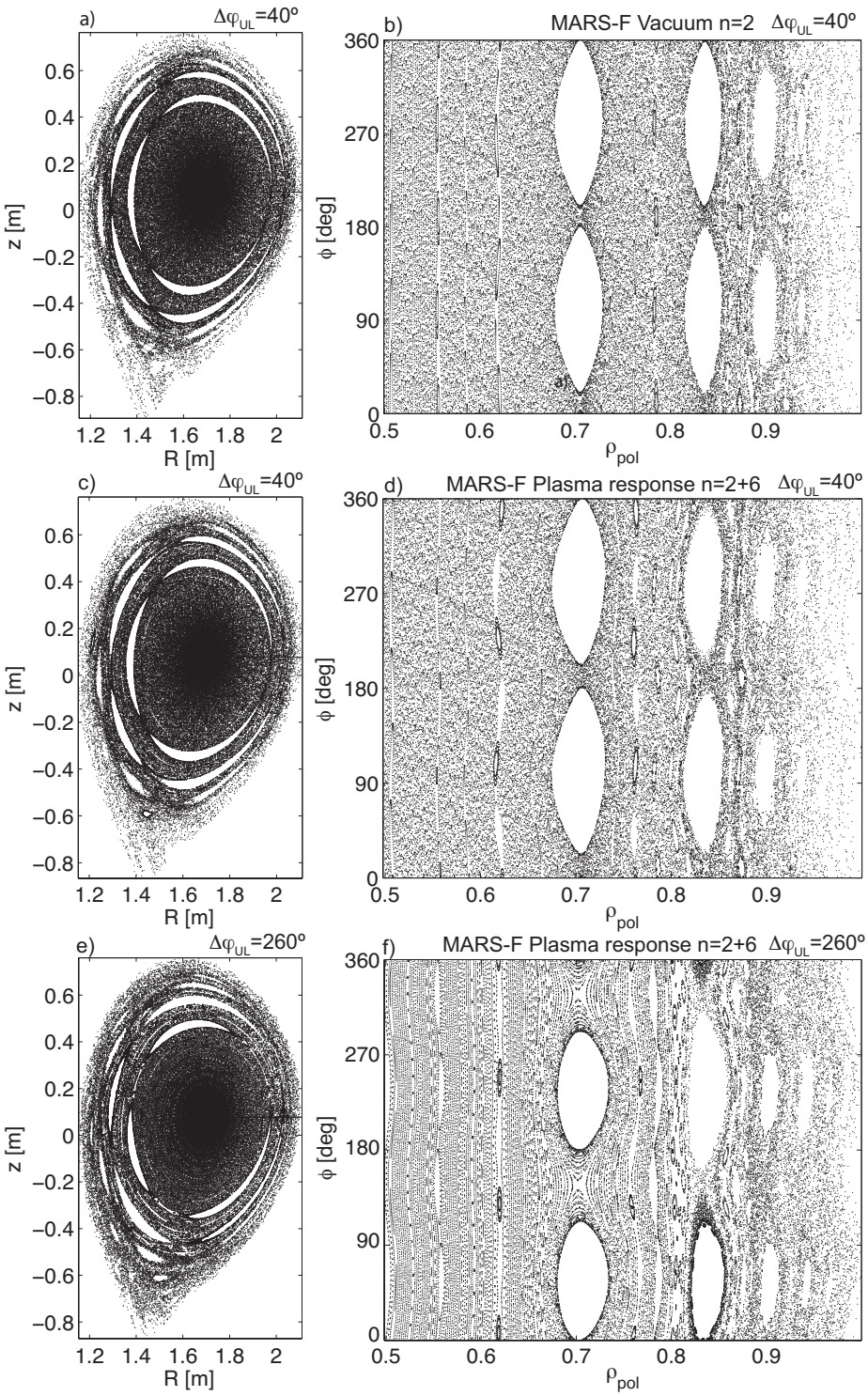

Figure 6.3: *Poloidal and toroidal Poincaré maps of the magnetic fields lines for different coil configurations corresponding to: a) and b)* $\Delta\varphi_{UL} = 40°$*, c) and d)* $\Delta\varphi_{UL} = 160°$ *and e) and f)* $\Delta\varphi_{UL} = 260°$.

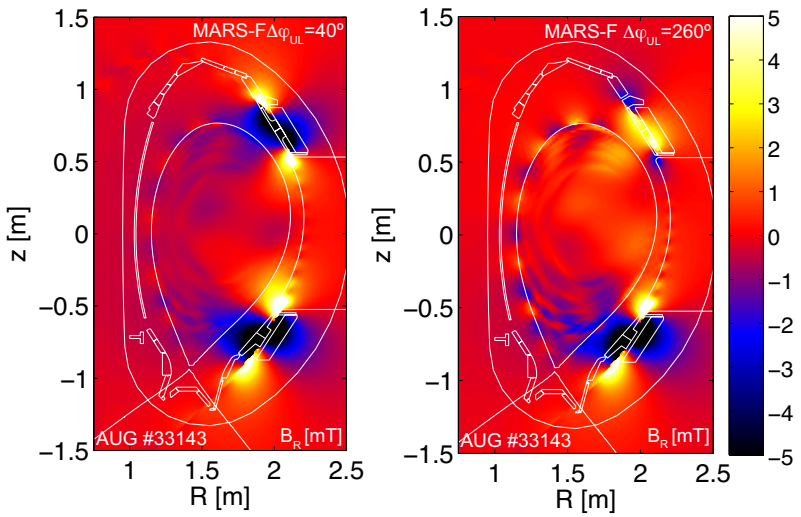

Figure 6.4: *Radial component of the RMP perturbative fields including the plasma response calculated by MARS-F for: a)* $\Delta\varphi_{UL} = 40°$ *and b)* $\Delta\varphi_{UL} = 260°$

6.1.3 Experimental validation

Using the calculated NBI#8 birth distribution and the different magnetic backgrounds, the fast-ion transport was calculated for 10 different time points covering the full range of the perturbation poloidal spectra. To relate each coil configuration to the associated time point, the rotational shielding of the magnetic perturbation caused by the currents induced in the PSL presented in figure 5.3 d) was taken into account. The particle trajectories were followed with ASCOT in full orbit motion using the leap-frog method with a time step of 10^{-9} s.

Figure 6.5 a) shows the total losses (normalised to their maximum) obtained with ASCOT for t=5 ms particle following time for each RMP configuration using the same initial particle distribution and n_e profile. All cases show a similar trend with the coils configuration, where a pure $n = 2$ perturbation in vacuum approach leads to a minimum of the losses and $n = 2, 6$ including the plasma response maximises the losses. These results also reveal that the impact of the plasma response on energetic particle losses changes with the RMP poloidal mode spectra. While the plasma response and vacuum approach for $n = 2, 6$ lead to similar fast-ion losses at $\Delta\varphi_{UL} = 260°$, the plasma response can increase the losses up to 20% at $\Delta\varphi_{UL} = 40°$. Excluding prompt losses, i.e. particles lost to the walls during the first poloidal

bounce, most of the losses induced by the 3D fields occur within the first 5 ms, so it can be assumed that the chosen following time is representative of the fast-ion loss behaviour.

Figure 6.5 b) shows the fast-ion losses measured with the FILD2 detector during these experiments. The AUG FILD2 system [73] is located above the midplane at z=0.30 m, R=2.19 m and $\phi = 123.5°$. The detector geometry allows the detection of particles within a pitch range between Λ=-0.9 and Λ=-0.1 and gyroradii between ρ_L=20 mm and ρ_L=120 mm. FILD measures fast-ion losses when the perturbation fields have a poloidal mode spectra between 100° and 200° with a maximum at $\Delta\varphi_{UL} = 150°$. A reasonable good agreement, see red curve in Figure 6.5 b), is obtained with ASCOT when filtering the lost particles that hit the FILD head, which is included as a 3D element of the AUG wall in ASCOT. The error bars in this figure were calculated as the standard deviation of a binomial process $\approx \sqrt{N}$, with N the number of ions reaching the FILD detector for each coil configuration. Charge-exchange losses were neglected in this numerical model and assumed not to play a key role in the understanding of the fast-ion transport dependency on the 3D fields configuration.

6.2 Edge Resonant Transport Layer

The experimental results show that the fast-ion transport in the presence of 3D fields depends on the poloidal mode spectra of the perturbation. Using the same model described to validate the numerical results against the experimental data, the induced fast-ion transport as a function of $\Delta\varphi_{UL}$ and the particle phase-space are analysed through the variation of the toroidal canonical momentum.

For a charged particle in a magnetic field, the toroidal canonical momentum (P_ϕ) is defined as:

$$P_\phi = mRv_\phi - Ze\Psi_{pol} \tag{6.1}$$

as introduced in chapter 2.4. Here, m is the particle mass, R is the particle

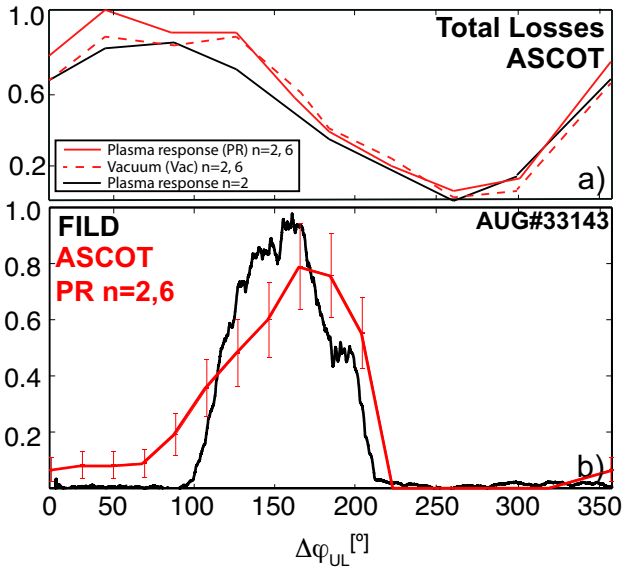

Figure 6.5: *a) Total fast-ion losses normalised to its maximum value as a function of* $\Delta\varphi_{UL}$ *including the n=2 plasma response (black), the n=2,6 plasma response (red) and the n=2,6 vacuum fields without the plasma response (red dashed line). b) Normalised values of measured (black) and simulated with ASCOT (red) FILD signals as a function of the applied* $\Delta\varphi_{UL}$.

major radius, v_ϕ is the toroidal component of the velocity, Ze is the particle charge and Ψ_{pol} is the poloidal magnetic flux. P_ϕ is a constant of motion for axisymmetric fields, but with the inclusion of non axisymmetric magnetic fields leading to a toroidal symmetry breaking, P_ϕ is not an invariant and its variation is associated to a radial transport of the particles. According to this definition, a positive variation in P_ϕ means that the particle is drifting inwards, while a negative variation leads the ion to drift outwards (see appendix A). The averaged variation of the fast-ion P_ϕ ($\langle \delta P_\phi \rangle$) was calculated as the time variation of P_ϕ averaged over approximately 10 bouncing motions as follows:

$$\langle \delta P_\phi \rangle = \frac{\sum_{i=1}^{N} (P_\phi(i) - P_\phi(0))}{N} \tag{6.2}$$

where $P_\phi(0)$ is the initial value of P_ϕ at t=0 s, i indicates different time points along the particle orbit and N is the total number of time points used for the average. Figure 6.6 a) shows $\langle \delta P_\phi \rangle$ as a function of the particle major radius and energy. Here, each point in the (R, E) grid, which is constituted by 40000 particles, was calculated by following each particle in full-orbit motion assuming a fixed initial gyrophase. An example of the temporal evolution of P_ϕ used to generate the $\langle \delta P_\phi \rangle$ plot is presented in figure 6.6 b). Here, P_ϕ shows a negative variation, which is associated to an outwards transport of the particle.

Figure 6.7 shows the energetic particle $\langle \delta P_\phi \rangle$ as a function of the initial particle pitch and plasma major radius for an energy of E=60 keV, initial z on the midplane and two different $\Delta\varphi_{UL}$.
Clear patterns appear for passing (Λ <-0.5 at R=2.0 m) and trapped (Λ >-0.5 at R=2.0 m) ions with a maximal $\langle \delta P_\phi \rangle$ located within 10 cm around the separatrix. The transport of trapped ions is dominated by resonant structures for all particle radial locations, while passing ions also show non-structured patterns from R=2.10 m. Indeed non-structured $\langle \delta P_\phi \rangle$ regions are observed mainly for passing ions with R$\geq$2.10 m, where the field line chaos at the plasma edge has a stronger impact. These structures also show a strong dependency with the particle initial pitch.

In order to identify the regions where 3D fields have an effect on fast-ion transport, figure 6.8 presents $\langle \delta P_\phi \rangle$ in the E-R plane considering the full radius range from the high field side to the low field side. This plot shows that the fast-ion transport due

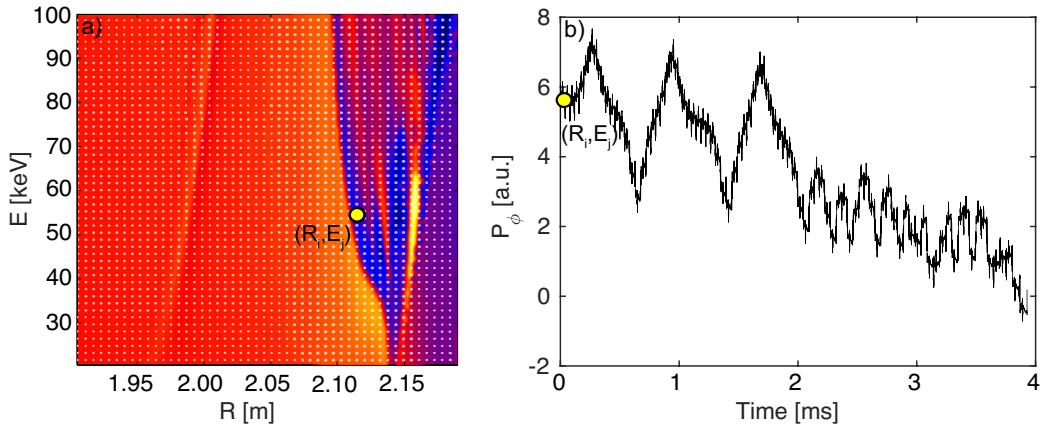

Figure 6.6: *a)* $\langle \delta P_\phi \rangle$ *as a function of the initial particle major radius and energy with an example of the input particle grid distribution (white points). b) Time evolution of a particle* P_ϕ *corresponding to initial coordinates (E, R) indicated by the yellow circle in figure a) with* $\Lambda = -0.5$ *and z=0 m.*

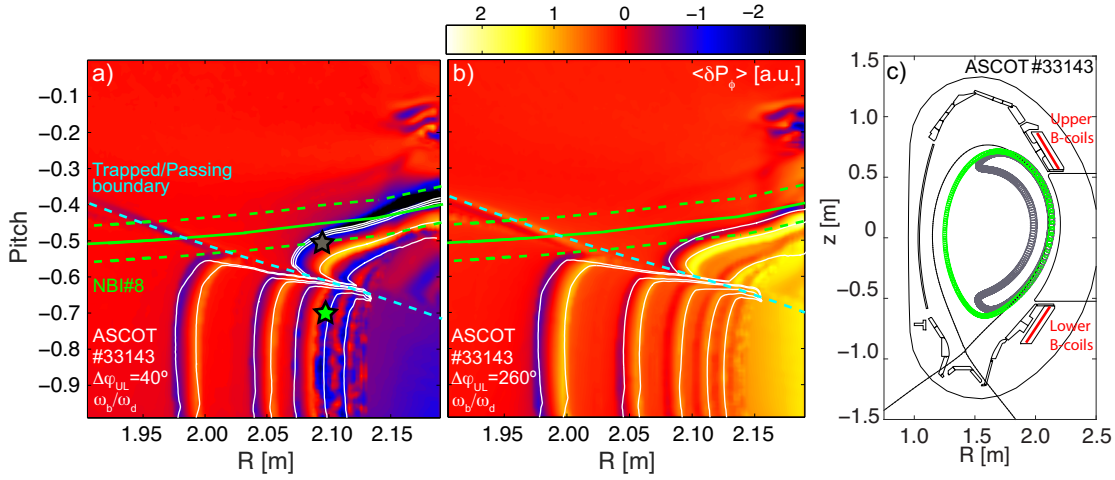

Figure 6.7: $\langle \delta P_\phi \rangle$ *as a function of particle pitch and plasma major radius for: a)* $\Delta\varphi_{UL} = 40°$ *and particle energy E=60 keV including the maximum of the NBI#8 birth distribution (green) and FWHM (dashed green) and b)* $\Delta\varphi_{UL} = 260°$*. White contours indicate the constant ratio of* $\omega_b/\bar{\omega}_d$ *and the cyan line shows the position of the boundary between passing and trapped orbits. Initial coordinates of passing (*$\Lambda = -0.7$*) and trapped (*$\Lambda = -0.5$*) orbits are marked with a star. c) Poloidal cross-section of the AUG vacuum vessel showing two unperturbed passing (green) and trapped (grey) particle orbits.*

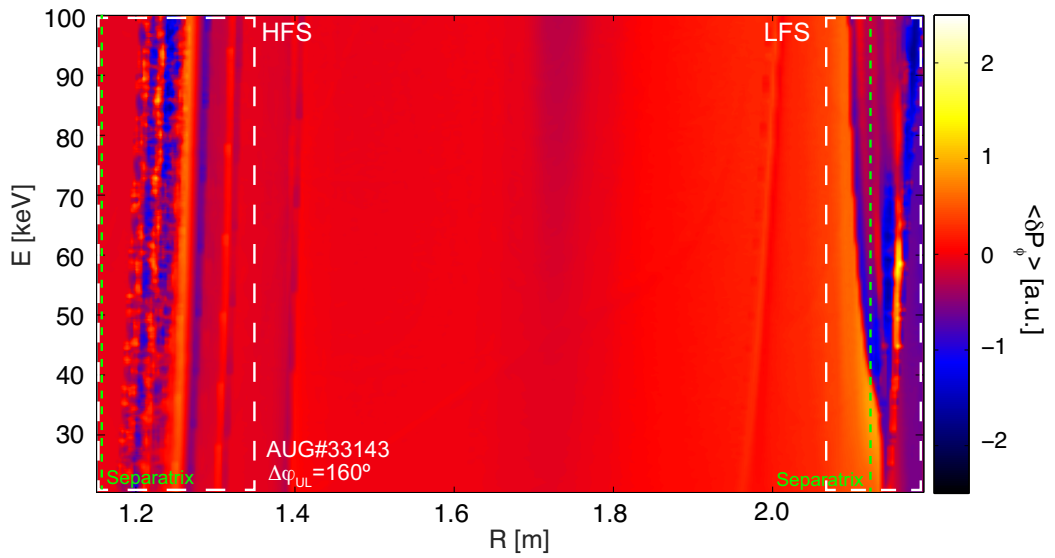

Figure 6.8: $\langle \delta P_\phi \rangle$ *as a function of the particle energy and particle major radius with initial coordinates* Λ*=-0.5 and* z*=0 m for* $\Delta\varphi_{UL} = 160°$*. Green dashed lines indicate the separatrix at the HFS and LFS* z*=0 m.*

to RMP fields is located close to the plasma edge in both the low field side (LFS) and high field side (HFS) while the inner plasma does not exhibit any transport structures.

The patterns observed in the $\langle \delta P_\phi \rangle$ plots can be understood by comparing them to the particle resonances. The static equilibrium for discharge AUG#33143 was used to calculate the particle resonances as the ratio between the bounce (ω_b) and precessional frequency ($\bar{\omega}_d$). In figures 6.9 a) and b) the frequency ratio has been plotted for both the HFS and LFS, respectively. At the LFS, which is mainly populated by trapped orbits, the frequency ratio exhibits a small gradient in the region close to the SOL corresponding to deeply trapped ions. This gradient increases towards the plasma core as it approaches the trapped/passing boundary, resulting in a region with very high resonance density. In the HFS region, where the population consists of passing orbits, the resonance gradient remains almost constant and the frequency ratio has a small dependency on the particle initial energy.

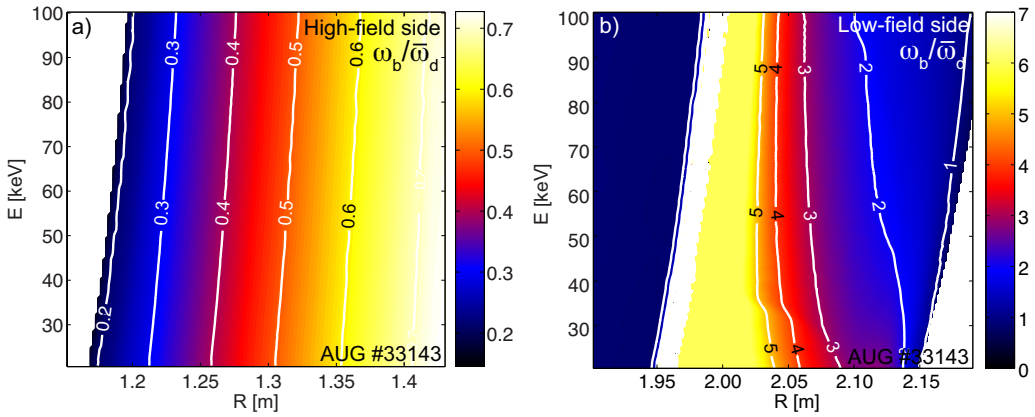

Figure 6.9: *Energetic particle resonances in an unperturbed equilibrium as a function of energy and particle major radius of a NBI#8 fast-ion distribution for: a) HFS using initial particle coordinates* $\Lambda = -0.7$*, z= 0 m and b) LFS using initial particle coordinates* $\Lambda = -0.5$*, z=0 m.*

6.2.1 Low field side

Figures 6.10 a)-d) show $\langle \delta P_\phi \rangle$ as a function of the particle energy and initial major radius with particle pitch Λ=-0.5 set by the NBI#8 injection geometry and initial z on the midplane at $z = 0\,m$. Here, $\langle \delta P_\phi \rangle$ was calculated through full orbit simulations for different coil configurations to show the impact of $\Delta\varphi_{UL}$ on energetic particle transport.
In figures 6.10 a)-d), clear transport structures are observed within 5 cm around the separatrix. The maximum in the simulated total losses presented in figure 6.5 a) for $\Delta\varphi_{UL} = 40°$ appears correlated with a maximum outward transport as figure 6.7 a) shows, while the minimum total losses for $\Delta\varphi_{UL} = 260°$ is related to the maximum inward transport in figure 6.10 c). Configurations $\Delta\varphi_{UL} = 160°$ and $\Delta\varphi_{UL} = 300°$ lead to intermediate total losses that are reflected in a moderate transport ($\langle \delta P_\phi \rangle$) as figures 6.10 b) and d) show.

By overplotting the particle resonances in the $\langle \delta P_\phi \rangle$ figures of merit, a clear matching between the maxima and minima in $\langle \delta P_\phi \rangle$ and particle resonances is found. This matching indicates that, when the perturbation is applied, the ERTL induces fast-ion transport through a combination of linear and nonlinear resonances. In this context, a particle resonance will be considered linear if the trajectory frequency ratio meets

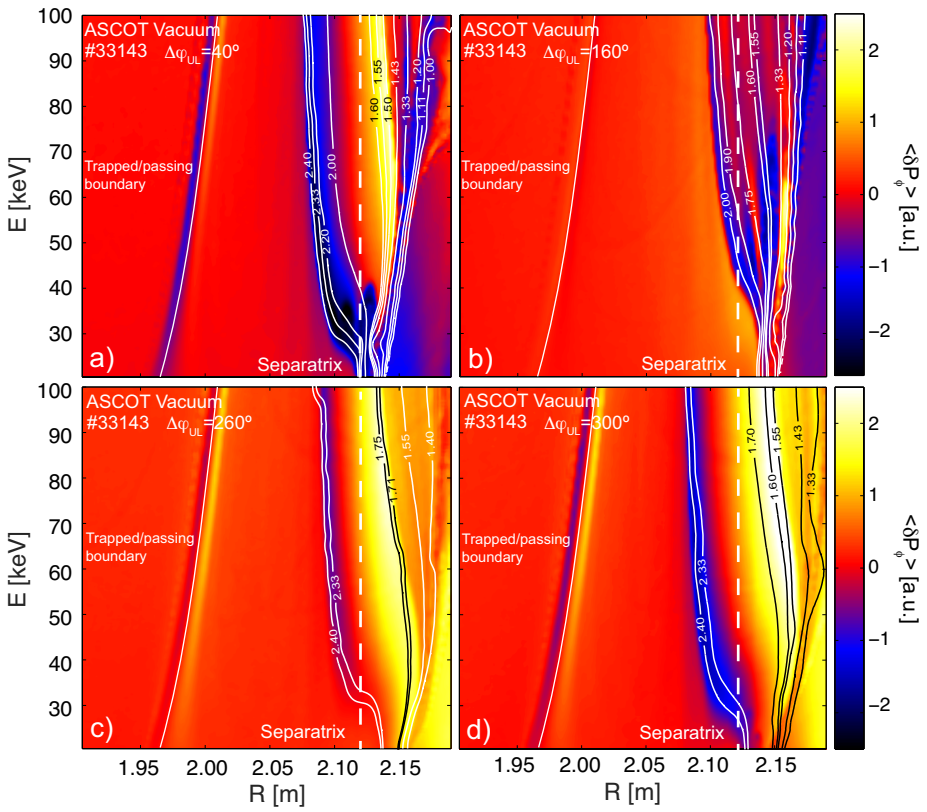

Figure 6.10: $\langle \delta P_\phi \rangle$ *as a function of particle major radius and energy for: a)* $\Delta\varphi_{UL} = 40°$*, b)* $\Delta\varphi_{UL} = 160°$*, c)* $\Delta\varphi_{UL} = 260°$ *and d)* $\Delta\varphi_{UL} = 300°$*. White contours indicate the particle frequency ratio* $(\omega_b/\bar{\omega}_d)$*.*

the condition $n\omega_b - p\bar{\omega}_d = 0$, where p is the bounce harmonic as described in section 3.1.

The particle resonances corresponding to a maximum variation of $\langle \delta P_\phi \rangle$ are $\omega_b/\bar{\omega}_d$=2.25 for $\Delta\varphi_{UL} = 40°$, $\omega_b/\bar{\omega}_d$=2 for $\Delta\varphi_{UL} = 160°$ and $\omega_b/\bar{\omega}_d$=1.75 for $\Delta\varphi_{UL} = 260°$. Near the trapped/passing boundary, the distance between consecutive resonances is reduced, which might cause a significant $\langle \delta P_\phi \rangle$ due to a resonance overlap in this region. From the set of particle resonances shown in figure 6.9, the ones responsible for the induced transport are located at the plasma edge, where the magnetic field is most affected by the 3D perturbation, as can be seen from the Poincaré maps in figure 6.3 at ρ_{pol}=0.85-1.00.

Figure 6.11 shows the radial profiles of $\langle \delta P_\phi \rangle$ corresponding to different $\Delta\varphi_{UL}$

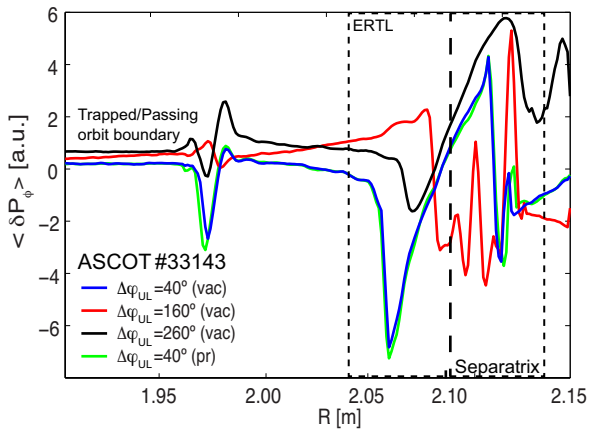

Figure 6.11: *Radial profiles of $\langle \delta P_\phi \rangle$ for different $\Delta\varphi_{UL}$ at energy of E=50 keV and pitch Λ=-0.5 considering vacuum approach and the plasma response.*

configurations along a fixed value of the energy at E=50 keV. This figure illustrates how $\Delta\varphi_{UL}$ can drastically change the transport intensity and the initial phase space of the resonant particles at the edge. The impact of the plasma response on the particle radial transport for this plasma discharge is shown in green for $\Delta\varphi_{UL} = 40°$ increasing the $\langle \delta P_\phi \rangle$ value by a maximum of 10%.

The role of initial toroidal phase is presented in figure 6.12, where $\langle \delta P_\phi \rangle$ is calculated for different $\Delta\varphi_{UL}$ indicating the NBI#8 injection and the position of the FILD detector. The structures in both configurations are dominated by the n=2 symmetry of the applied perturbation and the transport caused by multiple resonant interactions at the trapped/passing boundary. Figure 6.10 a) indicates that, for this configuration of $\Delta\varphi_{UL}$, the NBI#8 injection is the least favourable with respect to the perturbation as it injects particles with a set of initial particle coordinates very susceptible of being affected by RMP induced transport, while figure 6.10 c) shows the opposite.

6.2.2 High field side

On the magnetic HFS, the variation of $\langle \delta P_\phi \rangle$ shows a different pattern since the fast-ion population in this area consists of passing particles (figures 6.13 a)-d)). However, the variation of the poloidal mode spectra has a similar effect on the resonances responsible for the fast-ion transport, showing the maximum transport intensity at

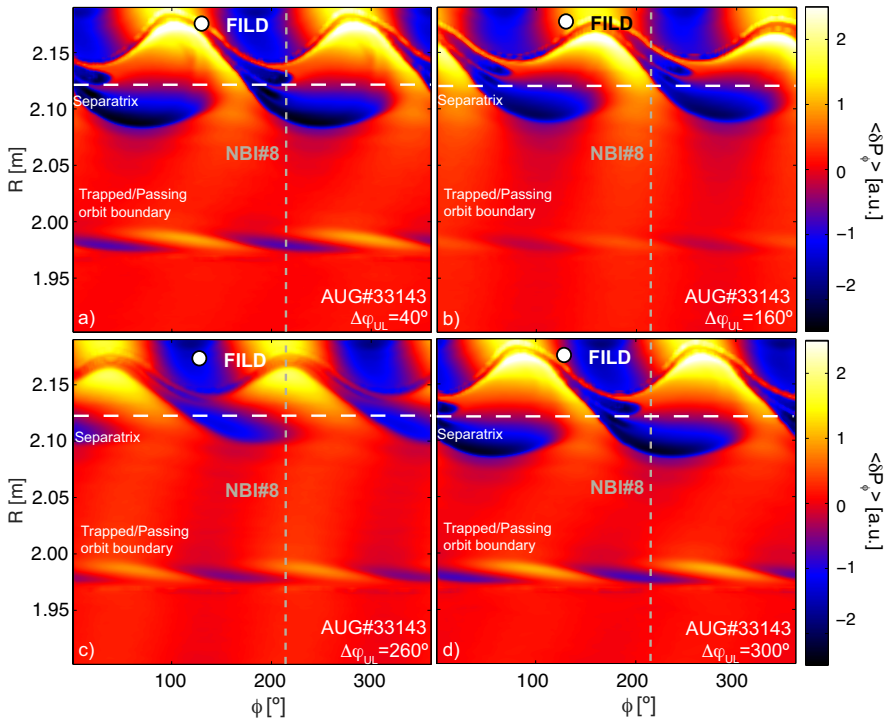

Figure 6.12: $\langle \delta P_\phi \rangle$ *plot showing the LFS area using a particle distribution with initial coordinates* Λ*=-0.5 and* z*=0 m as a function of plasma major radius and toroidal angle for: a)* $\Delta\varphi_{UL} = 40°$*, b)* $\Delta\varphi_{UL} = 160°$*, c)* $\Delta\varphi_{UL} = 260°$ *and d)* $\Delta\varphi_{UL} = 300°$*. The dashed gray line indicates the beam injection of NBI#8 and the location of the FILD detector is highlighted with a white circle.*

$\Delta\varphi_{UL} = 40°$ and minimum at $\Delta\varphi_{UL} = 260°$. The analysis of $\langle\delta P_\phi\rangle$ indicates that the transport is resonant in the core plasma region, but becomes chaotic as it approaches the separatrix due to the perturbation of the magnetic field lines, which has a large impact on the passing particles. The transport structure patterns and intensity observed in this region have a minimal dependency with the energy as was expected from the $\omega_b/\bar{\omega}_d$ ratio calculated in figure 6.9.

The calculation of $\langle\delta P_\phi\rangle$ as a function of the plasma major radius and toroidal angle (figure 6.14) shows a resonant structure (R=1.25-1.45 m) that is dominated by the n=2 toroidal mode number of the perturbation, which corresponds to the structures observed at the associated Poincaré maps (figure 6.3). In addition to the n=2 structures, a lobe structure is visible at the region closer to the separatrix and is more intense when the resonant magnetic configuration is applied at $\Delta\varphi_{UL} = 40°$. Note that these structures showing the fast-ion transport at the high-field side are very similar to the divertor heat flux patterns observed in the AUG measurements with similar coil configurations [77].

6.2.3 Resonant identification

The comparison between particle resonances and $\langle\delta P_\phi\rangle$ structures revealed that the fast-ion transport is caused by resonant interactions. By comparing the values of $\omega_b/\bar{\omega}_d$ to the $\langle\delta P_\phi\rangle$ structures, the resonances responsible for the transport could be identified. However, to understand the physics behind these values, each resonance in terms of the analytical theory of linear and nonlinear resonances presented in chapter 3 needs to be identified.

The ratio between the particle poloidal and toroidal frequencies required to meet the resonant condition when nonlinear effects are included is given by:

$$\frac{\omega_b}{\bar{\omega}_d} = \frac{n(l+1)}{p(l+1) \pm 1} \tag{6.3}$$

as it was described in chapter 3 for trapped particles. It can be used to identify resonances causing the fast-ion transport triggered by given values of $\Delta\varphi_{UL}$. In the

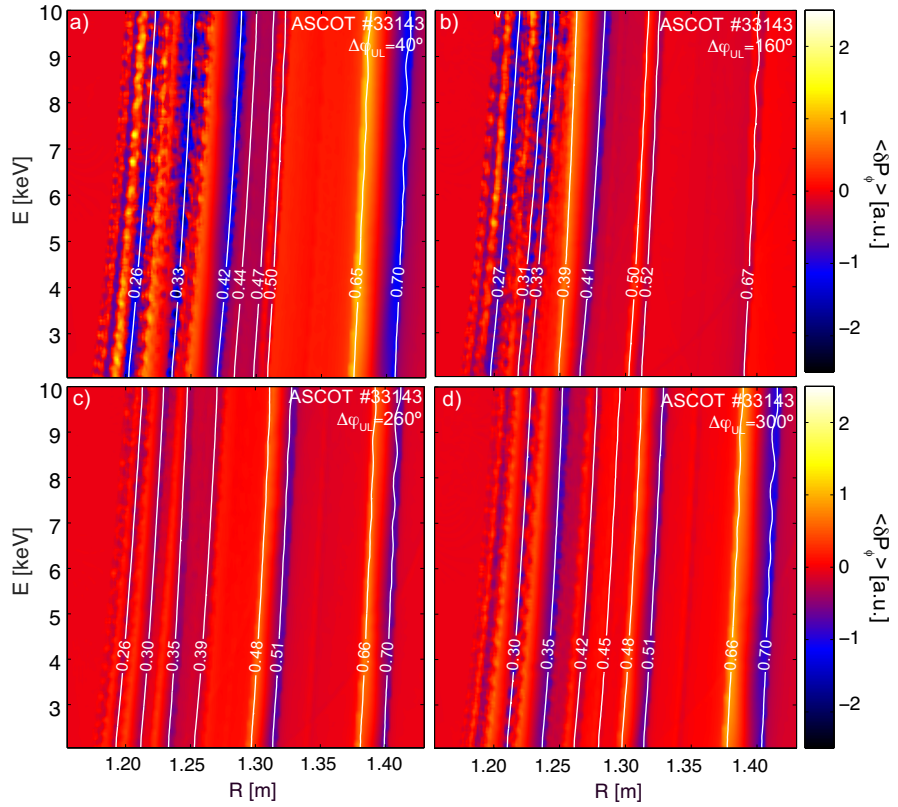

Figure 6.13: $\langle \delta P_\phi \rangle$ *on the HFS area as a function of plasma major radius and energy for particle initial coordinates* Λ*=-0.7 and* z*=0 m at: a)* $\Delta\varphi_{UL} = 40°$*, b)* $\Delta\varphi_{UL} = 160°$*, c)* $\Delta\varphi_{UL} = 260°$ *and d)* $\Delta\varphi_{UL} = 300°$*.*

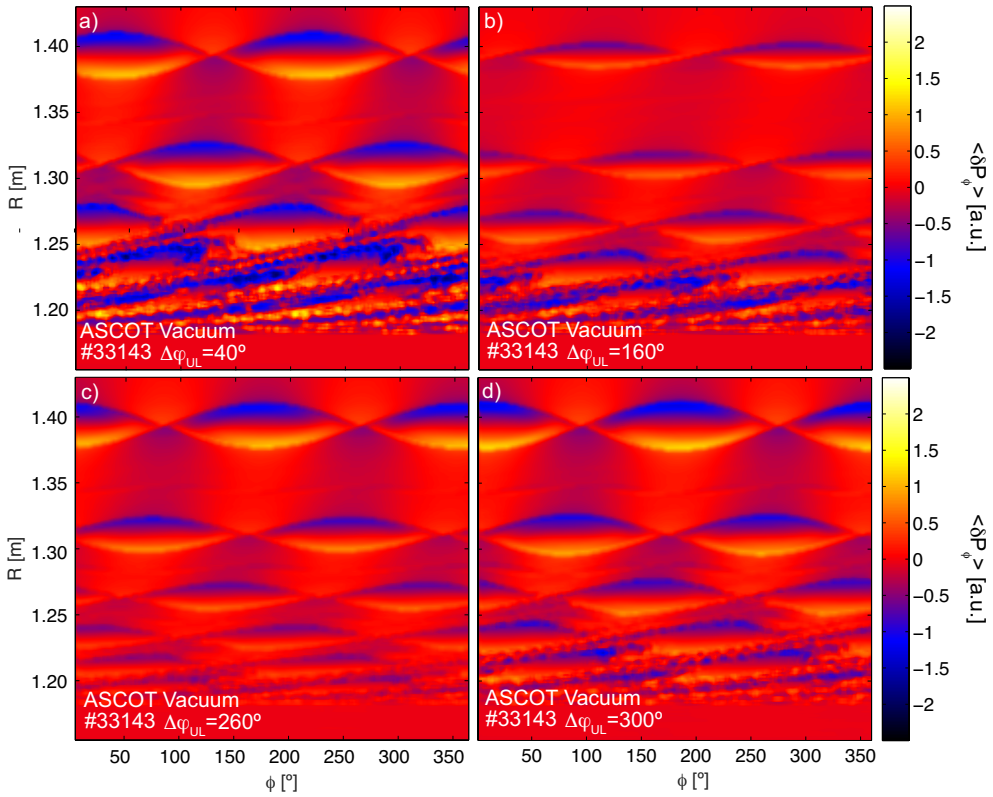

Figure 6.14: *Variation of* $\langle \delta P_\phi \rangle$ *on the HFS area as a function of plasma major radius and toroidal angle for particle initial coordinates* Λ*=-0.7 and* z*=0 m at: a)* $\Delta\varphi_{UL} = 40°$*, b)* $\Delta\varphi_{UL} = 160°$*, c)* $\Delta\varphi_{UL} = 260°$ *and d)* $\Delta\varphi_{UL} = 300°$*.*

analysed shot, n=2 is fixed due to the perturbation symmetry and p can take integer values reproducing most of the resonant structures in figure 6.10, where the amplitude and location of the selected resonance depends strongly on the frequency ratio.

Tables 6.1 and 6.2 contain the values of $\omega_b/\bar{\omega}_d$ corresponding to the main resonances found for each configuration together with the set of l, p_0 and p' parameters to generate each value. Although the particle transport is caused by both linear and nonlinear interactions, most of the resonances involved are observed to be nonlinear.

$\Delta\varphi_{UL} = 40°$					$\Delta\varphi_{UL} = 160°$				
$\omega_b/\bar{\omega}_p$	l	p_0	p'	n	$\omega_b/\bar{\omega}_d$	l	p_0	p'	n
1.00	0	2	0	2	1.00	0	2	0	2
1.11	4	2	1	2	1.11	4	2	1	2
1.20	2	2	1	2	1.20	2	2	1	2
1.33	1	2	1	2	1.33	1	2	1	2
1.50	2	1	1	2	1.50	2	1	1	2
1.60	3	1	1	2	1.60	3	1	1	2
2.00	0	1	0	2	1.75	6	1	1	2
2.33	6	1	-1	2	2.00	0	1	0	2
2.40	5	1	-1	2					

Table 6.1: *Set of l, p_0, p' and n corresponding to the identified resonances at $\Delta\varphi_{UL} = 40°$ and $\Delta\varphi_{UL} = 160°$.*

$\Delta\varphi_{UL} = 260°$					$\Delta\varphi_{UL} = 300°$				
$\omega_b/\bar{\omega}_p$	l	p_0	p'	n	$\omega_b/\bar{\omega}_d$	l	p_0	p'	n
1.50	2	1	1	2	1.33	1	2	1	2
1.71	5	1	1	2	1.60	3	1	1	2
1.75	6	1	1	2	1.71	5	1	1	2
2.33	6	1	-1	2	2.33	6	1	-1	2
2.40	5	1	-1	2	2.40	5	1	-1	2

Table 6.2: *Set of l, p_0, p' and n corresponding to the identified resonances at $\Delta\varphi_{UL} = 260°$ and $\Delta\varphi_{UL} = 300°$.*

As the HFS region is populated by passing ions, the q value ($q = \langle d\phi/d\theta \rangle$) of the magnetic field associated to the initial radial location of the particle, is approximately similar to the inverse of the frequency ratio ($\bar{\omega}_d/\omega_b$) presented in figures 6.13 a)-d).

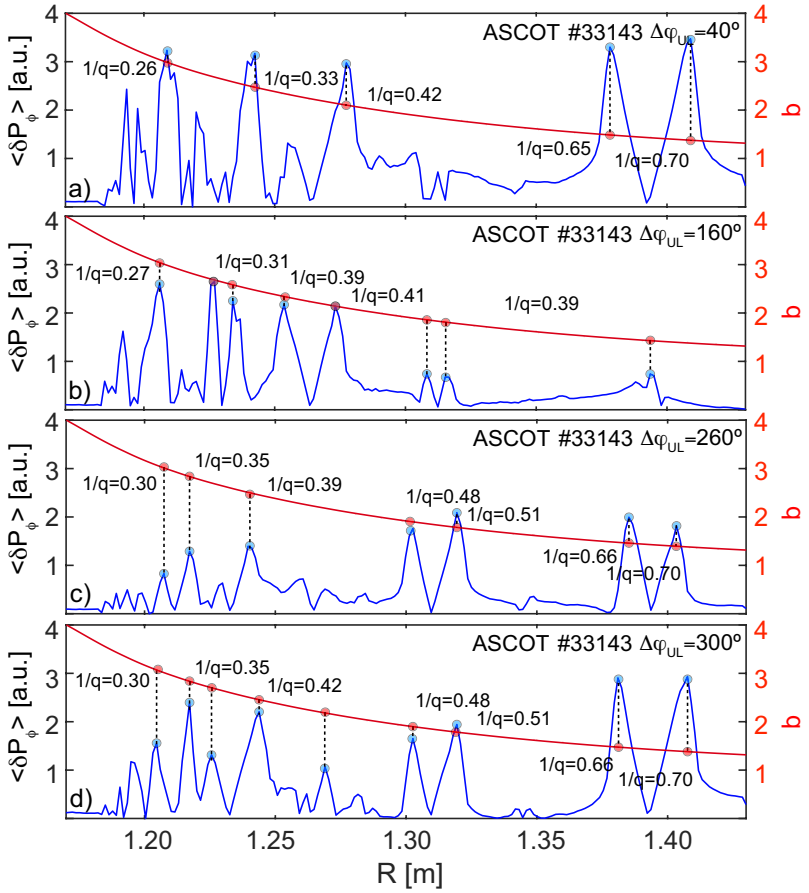

Figure 6.15: $|\langle \delta P_\phi \rangle|$ *profile at energy E=40 keV (blue) and q-profile (red) as a function of plasma major radius for: a)* $\Delta\varphi_{UL} = 40°$*, b)* $\Delta\varphi_{UL} = 160°$*, c)* $\Delta\varphi_{UL} = 260°$ *and d)* $\Delta\varphi_{UL} = 300°$.

In this case, the determination of the frequency ratio was made by means of the identification of the $1/q$ values corresponding to the maxima in the $\langle \delta P_\phi \rangle$ radial profile at a fixed value of the energy. Figure 6.15 shows how each peak of the $\langle \delta P_\phi \rangle$ profile was associated to the inverse of q at the corresponding radial location, generating the $\bar{\omega}_d/\omega_b$ value observed in figure 6.13.

6.3 Characterisation of the ERTL

Using the description of the ERTL as the region where fast-ion transport is maximised in the presence of a 3D perturbation, more extensive analysis on the dependencies with the main plasma and operation parameters is presented in terms of $\langle \delta P_\phi \rangle$.

6.3.1 Perturbation amplitude

A scan in the amplitude of the magnetic perturbation was used to analyse its effects on linear and nonlinear resonances (figures 6.16 a)-c)). For amplitude levels routinely used for ELM mitigation, both linear and nonlinear resonances cause particle transport, but the resonant transport is mainly nonlinear (figure 6.17 a)). As the amplitude decreases, the intensity of nonlinear resonances ($l \neq 0$) becomes weaker (figure 6.17 b)) until they completely disappear and linear resonances are the dominant transport mechanism (figure 6.17 c)). This fading of the $\langle \delta P_\phi \rangle$ structures is summarized in figure 6.17 a), where structures associated to linear resonances (marked with blue circles) are the only peaks that remain when the perturbation amplitude decreases.

A more detailed description of the difference in the behaviour of linear and non linear resonances is presented in figure 6.17 b), where the intensity of $\langle \delta P_\phi \rangle$ is shown as a function of the perturbation amplitude. By comparing the increasing trends, $\delta B \times 0.55$ is observed to be the value delimiting the regions where linear and non linear resonances are dominant.

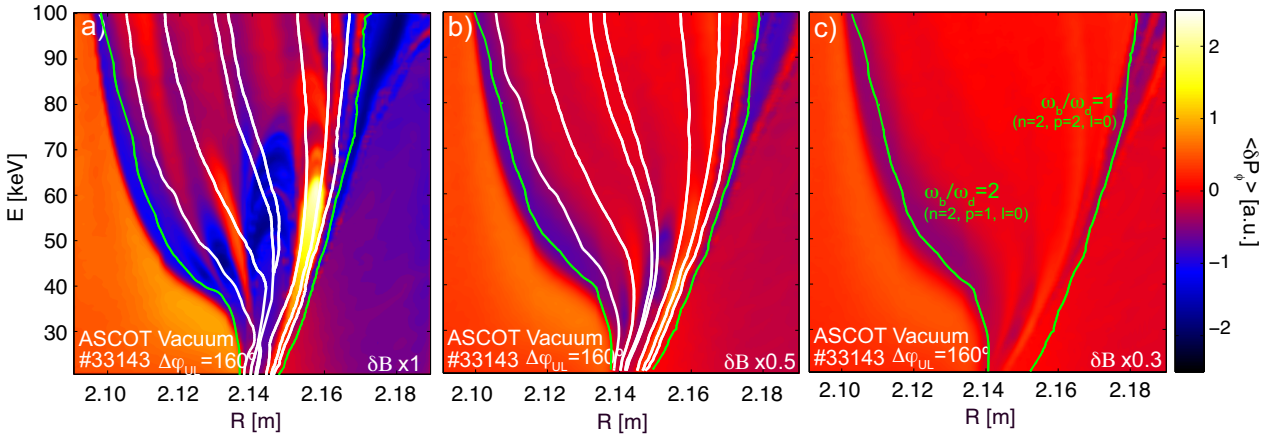

Figure 6.16: $\langle \delta P_\phi \rangle$ *calculated for* $\Delta\varphi_{UL} = 160°$ *coil configuration for a particle distribution initialised at* Λ*=-0.5 and* z*=0 m using 3D field amplitude of: a)* $\delta B \times 1$ *(amplitude value from the measured coil currents), b)* $\delta B \times 0.5$ *and c)* $\delta B \times 0.3$*. Contours indicate the* $\omega_b/\bar{\omega}_d$ *ratio for linear (green) and nonlinear (white) resonances.*

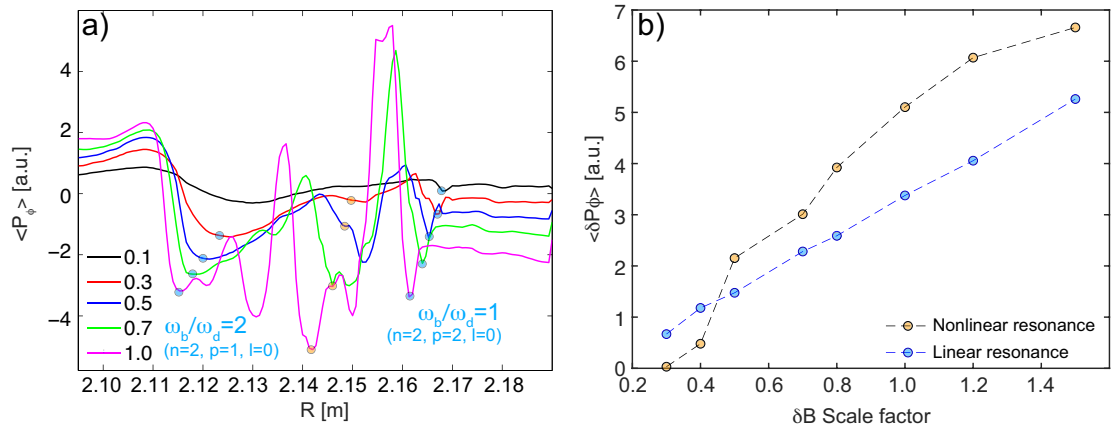

Figure 6.17: *a)* $\langle \delta P_\phi \rangle$ *profiles for* $\Delta\varphi_{UL} = 160°$ *configuration at energy* E*=50 keV using different* δB *amplitudes where linear resonance* n*=2,* p_0*=2 is indicated by a blue circle and nonlinear resonance* n*=2,* p_0*=1,* p'*=1,* l*=3 indicated by an orange circle. b)* $\langle \delta P_\phi \rangle$ *as a function of* δB *for a linear resonance (blue) and non linear resonance (yellow).*

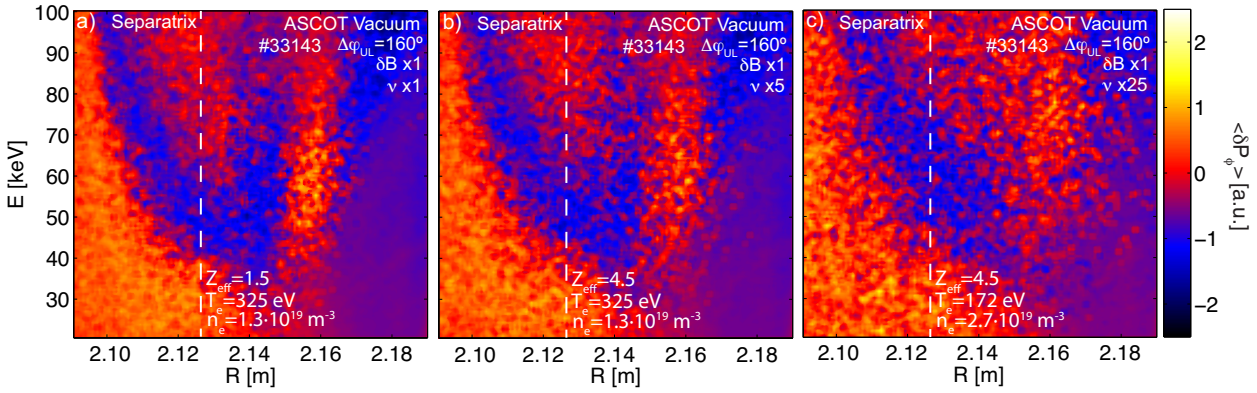

Figure 6.18: $\langle \delta P_\phi \rangle$ *calculated for* $\Delta\varphi_{UL} = 160°$ *coil configuration for a particle distribution initialised at* Λ*=-0.5 and* z*=0 m including collisions for increasing values of electron collisionality* ν_e^*.

6.3.2 Coulomb collisions

The impact of Coulomb collisions on the $ERTL$ is also assessed through realistic simulations including collisions between fast-ions and the bulk plasma where particle orbits have been traced using the same following time as in figure 6.16 to show the effect of collisions within the same time scale. The ASCOT collision operator includes pitch scattering [26] and uses a realistic value of the effective ion charge (Z_{eff}) to determine the collision rates. Figure 6.18 a) shows $\langle \delta P_\phi \rangle$ including Coulomb collisions considering the plasma parameters corresponding to shot AUG#33143. In order to analyse the impact of collisionality on the transport structures, the electron collisionality was changed by modifying the values of ion temperature, density and Z_{eff} as presented in figures 6.18 b) and c). The effect of increasing the collisionality on the $ERTL$ leads to a widening of the resonances, but also to an overall decrease of the $\langle \delta P_\phi \rangle$ peak structure associated to the individual resonances.

6.3.3 Radial electric field

The effect of the radial electric field on the ERTL was also studied by means of $\langle \delta P_\phi \rangle$ as a function of the particle initial phase space and the strength of the E_r profile. The electric field used for these simulations, shown in figure 6.19 a), was calculated based on experimental measurements for shot AUG#33143 from the magnetic axis

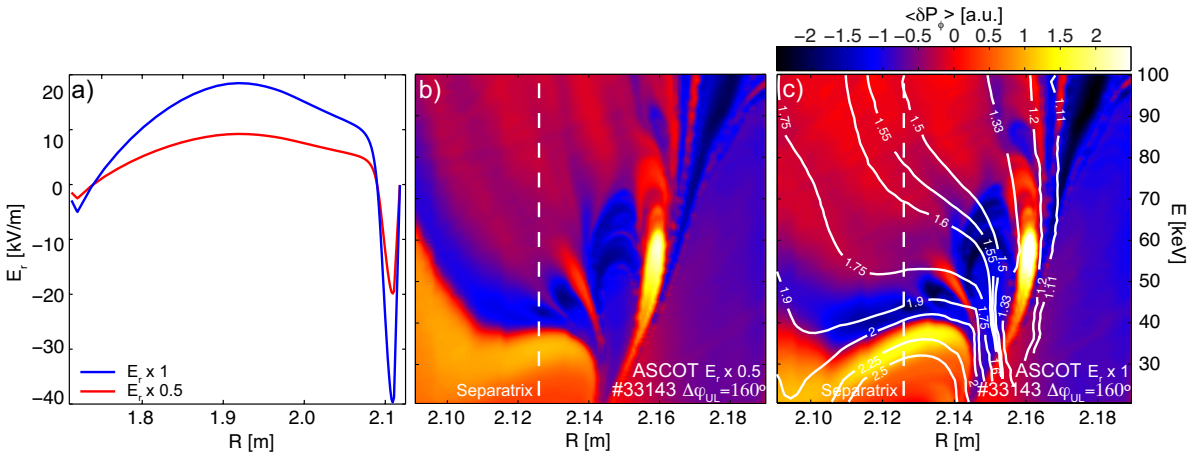

Figure 6.19: *a) Radial electric field profile derived from AUG experimental measurements. b) and c)* $\langle \delta P_\phi \rangle$ *calculated for* $\Delta\varphi_{UL} = 160°$ *coil configuration including the radial electric field as* $E_r/2$ *and* E_r *respectively for particle initial coordinates* Λ*=-0.5 and z=0 m. White contours indicate the particle frequency ratio* $\omega_b/\bar{\omega}_d$.

to the separatrix, showing the common behaviour observed in H-mode plasmas [78]. Figures 6.19 b) and c) show $\langle \delta P_\phi \rangle$ considering the electric field for two values of E_r including $E_r \times 0.5$ and $E_r \times 1$, respectively.

As can be observed from the comparison between figures 6.19 b) and 6.16 a), the impact of the radial electric field is to distort the resonant structures at the location of the E_r well, but it can also alter a small region outside the separatrix. This effect is related to the topology of trapped orbits, where ions born outside the separatrix can also explore inner regions of the plasma on the inner banana orbit leg. The orbital frequency ratio $\omega_b/\bar{\omega}_d$ was calculated including the E_r in figure 6.19 c), showing that the distortion of the $\langle \delta P_\phi \rangle$ structures matches the new frequency ratio. Considering this, it can be assumed that equation 6.3 is still valid in the presence of E_r.

Although the structures are altered, the maximum variation of $\langle \delta P_\phi \rangle$ is not changed. Also, due to the distortion of the resonances, the transport associated to $\langle \delta P_\phi \rangle$ at high energies is eliminated, which might lead to a better ion confinement for this coil configuration.

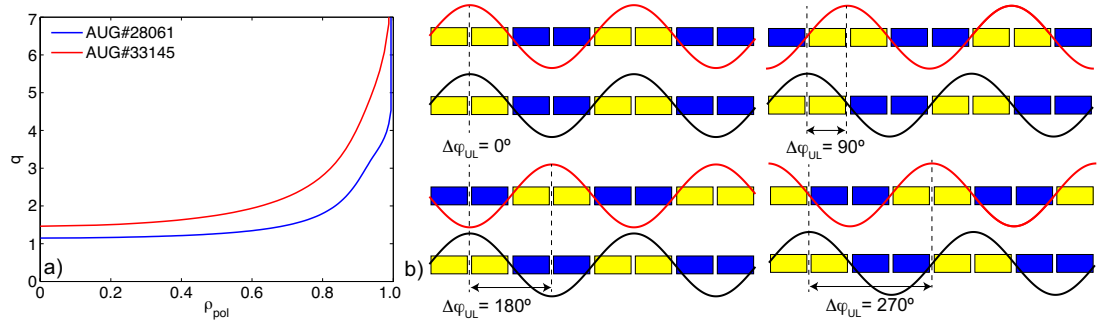

Figure 6.20: *a) Safety factor profile for discharges AUG#33145 (red) and AUG#28061 (blue). b) Coil configuration corresponding to the different* $\Delta\varphi_{UL}$ *applied.*

6.3.4 Magnetic equilibrium

For the sake of simplicity, only one discharge was used to illustrate the different dependencies of the ERTL. The results presented here are, however, applicable to all AUG plasma discharges with MPs. The ERTL was analysed for two additional discharges, AUG#33145 with a plasma current of I_p=0.7 MA, toroidal magnetic field B_ϕ=-2.5 T and AUG#28061 with a plasma current of I_p=0.8 MA, toroidal magnetic field B_ϕ=-1.8 T. Figure 6.20 a) shows the safety factor profiles corresponding to both discharges and figure 6.20 b) shows the different coil configurations used to assess the impact of the perturbation mode spectra on both equilibria.

In agreement with the previous results, figures 6.21 and 6.22 show that the $\Delta\varphi_{UL}$ plays a key role in the observed overall particle transport. Here, it is important to note that the $\Delta\varphi_{UL}$ responsible for the minimum/maximum particle transport depends on the magnetic equilibrium. For the AUG#33145 equilibrium, the coil configuration leading to the maximum outwards transport corresponds to $\Delta\varphi_{UL} = 180°$, while for discharge AUG#28061 the maximum transport occur at $\Delta\varphi_{UL} = 0°$. The analysis of the ERTL allows to chose the MP configuration together with the magnetic equilibrium such that fast-ion transport is minimised.

Safety factor

The effect of the equilibrium q profile on the ERTL was analysed through discharges AUG#28061 and AUG#28059. The two shots selected for this study had similar

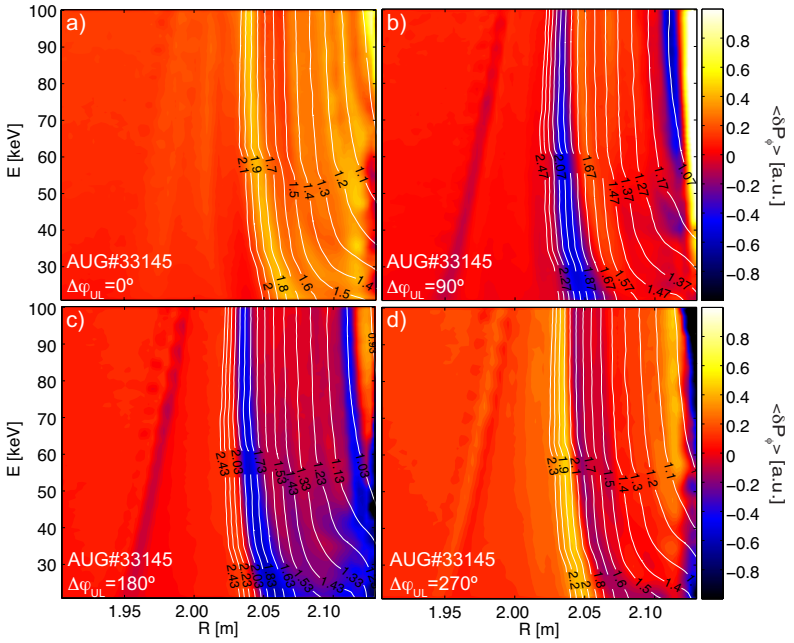

Figure 6.21: *AUG# 33145.* $\langle \delta P_\phi \rangle$ *on the LFS area as a function of plasma major radius and energy for particle initial coordinates* Λ*=-0.5 and* z*=0 m at: a)* $\Delta\varphi_{UL} = 0°$*, b)* $\Delta\varphi_{UL} = 90°$*, c)* $\Delta\varphi_{UL} = 180°$ *and d)* $\Delta\varphi_{UL} = 270°$.

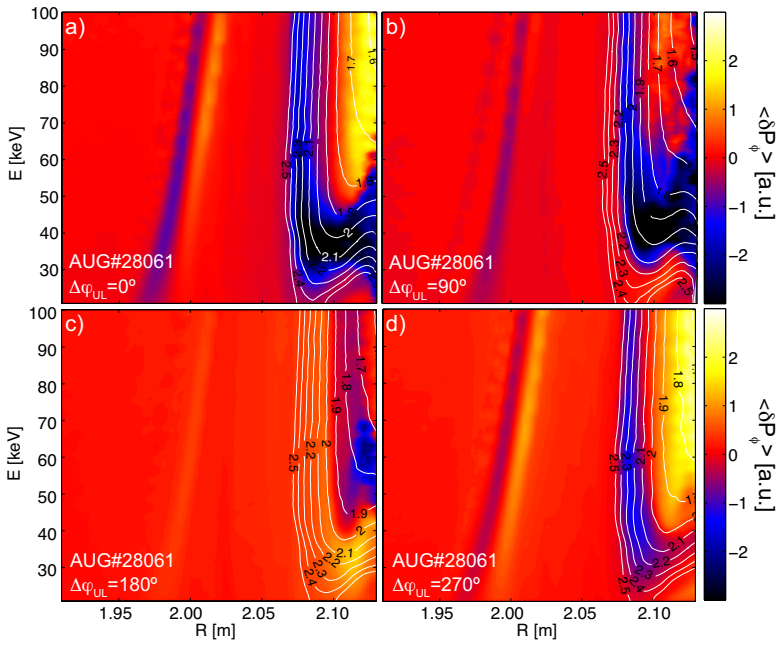

Figure 6.22: *AUG# 28061.* $\langle \delta P_\phi \rangle$ *on the LFS area as a function of plasma major radius and energy for particle initial coordinates* Λ*=-0.5 and z=0 m at: a)* $\Delta\varphi_{UL} = 0°$*, b)* $\Delta\varphi_{UL} = 90°$*, c)* $\Delta\varphi_{UL} = 180°$ *and d)* $\Delta\varphi_{UL} = 270°$*.*

plasma shapes to ensure that both equilibria had the separatrix located at the same radial location as shown in figure 6.23. The q profiles corresponding to each magnetic equilibrium are presented in figure 6.24 a).

Figure 6.24 b) shows the coil configuration corresponding to $\Delta\varphi_{UL} = 180°$ applied to both equilibria to calculate the $\langle \delta P_\phi \rangle$ presented in figures 6.24 c) and 6.24 d). The observed impact of the q profile on the ERTL is a displacement of the resonances towards the plasma core for higher values of q. This effect can be clearly identified in the $\langle \delta P_\phi \rangle$ radial profiles shown in figure 6.24, where the maximum intensity of the fast-ion transport is shifted inwards for AUG#28059 with higher q profile.

6.3.5 Toroidal symmetry of the magnetic perturbation

A similar analysis has been done using different toroidal symmetries for the 3D perturbative fields, more specifically, the $n = 4$ symmetry has been analysed for discharge AUG#34570. Figure 6.26 a) and b) shows $\langle \delta P_\phi \rangle$ for poloidal spectra

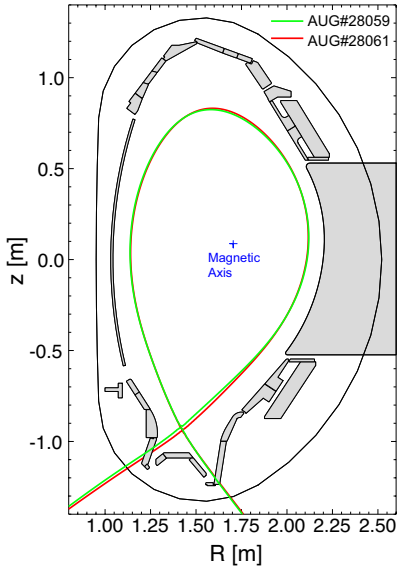

Figure 6.23: *Poloidal cross-section of AUG showing the separatrix corresponding to AUG#28061 (red) and AUG#28059 (blue) equilibria at t=2.00 s.*

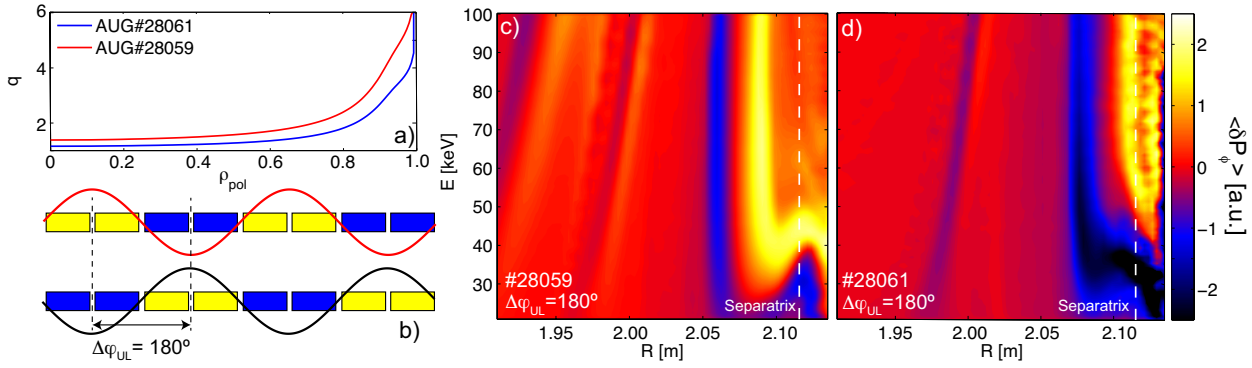

Figure 6.24: *a) Safety factor profile for discharges AUG#28061 (blue) and AUG#28059 (red). b) Coil configuration corresponding to* $\Delta\varphi_{UL} = 180°$. $\langle\delta P_\phi\rangle$ *on the LFS area as a function of plasma major radius and energy for particle initial coordinates* Λ*=-0.5 and z=0 m and* $\Delta\varphi_{UL} = 180°$ *for: c) AUG#28059 and d) AUG#28061*

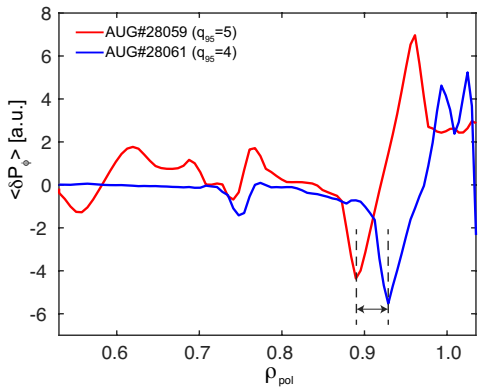

Figure 6.25: *Radial profiles of* $\langle \delta P_\phi \rangle$ *for* $\Delta\varphi_{UL} = 180°$ *at energy of* $E = 50\,keV$ *and pitch* $\Lambda = -0.5$ *for discharges AUG#28061 (blue) and AUG#28059 (red).*

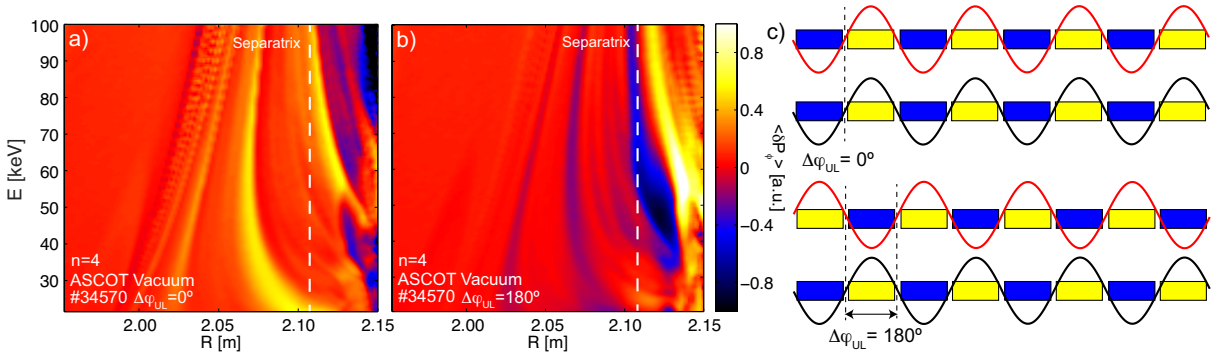

Figure 6.26: *AUG#34570.* $\langle \delta P_\phi \rangle$ *on the LFS area as a function of plasma major radius and energy for particle initial coordinates* Λ*=-0.5 and z=0 m for: a)* $\Delta\varphi_{UL} = 0°$ *and b)* $\Delta\varphi_{UL} = 180°$*. c) Coil configuration for* $\Delta\varphi_{UL} = 0°$ *and* $\Delta\varphi_{UL} = 180°$ *using an* $n = 4$ *toroidal symmetry.*

$\Delta\varphi_{UL} = 0°$ and $\Delta\varphi_{UL} = 180°$ corresponding to the coil configurations shown in figure 6.26 c). The fast-ion transport observed for the $n = 4$ case is also located at the plasma edge and has a dependence on the perturbation poloidal spectra.

6.3.6 Convergence tests

The simulation parameters used throughout this section were carefully chosen from the results of several convergence tests in different grid resolution, following time, integration step and time points used to calculate $\langle \delta P_\phi \rangle$.

- Particle integration time step

  To optimise the time step Δt_{step} set for the leap-frog integration method, $\langle \delta P_\phi \rangle$ was calculated using different values. Figure 6.27 a)-c) show $\langle \delta P_\phi \rangle$ using three values of Δt_{step}. The location and shape of the structures does not change, however, the intensity of $\langle \delta P_\phi \rangle$ in figure 6.27 a) presents a noticeable variation with respect to figures 6.27 b) and c). In order to save as much cpu-time as possible, $\Delta t_{step} = 10^{-9}\, s$ was chosen as an increased value shows a very similar result.

- Grid resolution

  The dependency on the initial particle grid size was also analysed by increasing the grid resolution by a factor of 2. Figure 6.27 d) shows the increased grid compared to 6.27 b) which was made using the regular 40000 particle resolution. These plots show that doubling the grid size does not provide any relevant information about the shape or intensity of the $ERTL$ structures.

- Particle following time

  Figure 6.28 shows $\langle \delta P_\phi \rangle$ using different particle following time Δt_{ft} from 0.3 ms to 5 ms. The effect of increasing Δt_{ft} on the $ERTL$ structures inside the separatrix is weak and only observed in the $\langle \delta P_\phi \rangle$ intensity. The resonant structures outside the separatrix exhibit a similar pattern with an increased intensity, but as it only affects a region with a very low particle population, it is not significative in the description of NBI fast-ion transport.

- Number of time points to calculate $\langle \delta P_\phi \rangle$

  In all presented $\langle \delta P_\phi \rangle$ plots, the averaged variation of P_ϕ is calculated according to expression 6.2, where N was defined as the total number of time points along the particles trajectory used. As only the information of the selected time

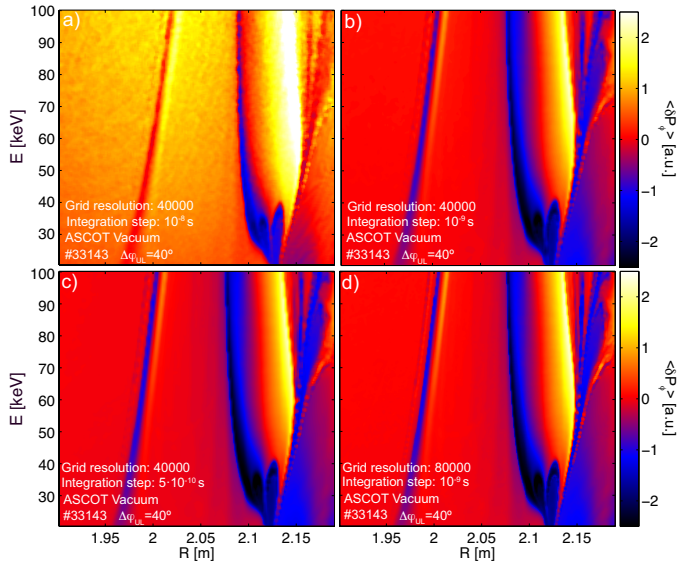

Figure 6.27: $\langle \delta P_\phi \rangle$ *as a function of energy and initial radial position using particle pitch* $\Lambda = -0.5$ *and* $z = 0\,m$ *for: a)-c) different integration steps and d) different grid particle resolution.*

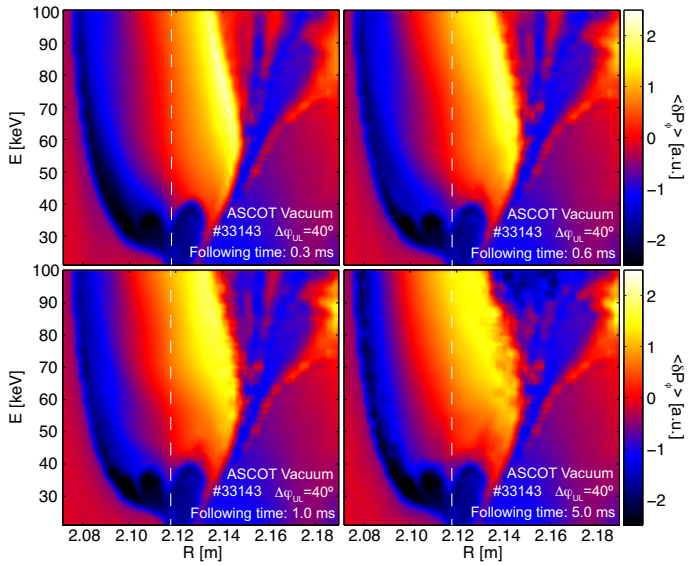

Figure 6.28: $\langle \delta P_\phi \rangle$ *as a function of energy and initial radial position using particle pitch* $\Lambda = -0.5$ *and* $z = 0\,m$ *for different values of* Δt_{ft}.

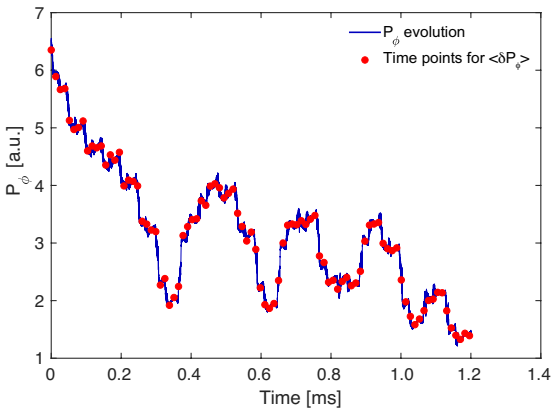

Figure 6.29: *Time evolution of P_ϕ showing in red the time points N considered to calculate the averaged variation of P_ϕ using $\Delta t_{step} = 10^{-9}\,s$.*

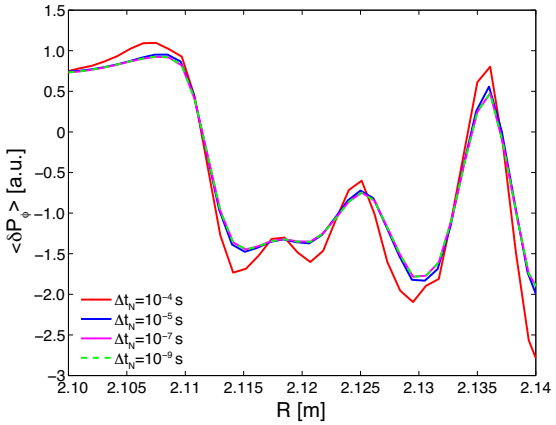

Figure 6.30: *Radial profile of $\langle \delta P_\phi \rangle$ at energy E=40 keV for different time intervals Δt_N using a $\Delta \varphi_{UL} = 40°$.*

points is needed to calculate $\langle \delta P_\phi \rangle$, the rest of the trajectory is not stored. Note that this does not affect the integration time of the orbit, which is set to $10^{-9}\,s$. Figure 6.29 shows $P_\phi(t)$ in blue and the red circles indicate the selected time points included in equation 6.2.

The time interval between each point Δt_N was tested for different values to find the optimal value to avoid storing unnecessary data. In figure 6.30 the radial profile of $\langle \delta P_\phi \rangle$ is presented using Δt_N values from $10^{-4}\,s$ to $10^{-9}\,s$ showing that $\Delta t_N = 10{-}5$ is the minimal value required to calculated $\langle \delta P_\phi \rangle$ accurately.

Chapter 7

Summary and Discussion

This work identifies the Edge Resonant Transport Layer as the region which involves the resonant transport responsible for the fast-ion losses in the presence of externally applied 3D fields in a tokamak. This theoretical explanation for the fast-ion transport is supported by ASCOT numerical simulations capable of reproducing experimental results qualitatively.

The resonant transport studied in this work has been assessed through the variation of the toroidal canonical momentum, which is related to a radial drift on the ion orbit in the presence of 3D fields. By analysing the $\langle \delta P_\phi \rangle$ for different magnetic configurations, covering a full scan in the perturbation poloidal spectra, it has been observed that the transport occurs due to resonant wave-particle interactions within 10 cm around the plasma edge. This ERTL depends on the fast-ion orbit topology, perturbation spatial spectrum and amplitude as well as the plasma collisionality. The associated resonant structures in the phase-space appear on both the HFS and LFS.

An analytical expression to describe the resonant condition for nonlineal interactions has been derived and used to identify the resonances responsible for the particle transport observed in the ASCOT simulations.

These resonant transport structures in the particle phase-space have been char-

acterised in terms of the amplitude of the externally applied magnetic perturbations. It has been observed that the dominant resonant transport is linear for small amplitude perturbations, but it becomes nonlinear as the amplitude increases to levels used routinely for RMP ELM suppression.

When Coulomb collisions are included, the interaction with the bulk plasma causes a variation of the particle velocity, which leads to a breaking of the wave-particle resonance condition and, as a consequence, the particle transport decreases.

The effects of the radial electric field have also been studied using different amplitudes of E_r, observing a distortion of the $ERTL$ structures. However, the location of the resonant transport remains at the plasma edge and the intensity of the $\langle \delta P_\phi \rangle$ associated to the radial transport does not change significantly.

The $\langle \delta P_\phi \rangle$ was calculated using different toroidal symmetries for the external perturbations which led to similar resonant structures in agreement with the previous results. The impact of a change in the safety factor was analysed. A inwards radial shift in the phase-space of the resonant particles for higher values of the safety factor was observed.

The results discussed in this work were used to shed light on the nature of the fast-ion transport mechanism involved in the analysed experiment. The modelling tools developed in this thesis can also be utilised to predict the energetic particle confinement in current and future devices like ITER. Based on this, the analysis of $\langle \delta P_\phi \rangle$ can be applied to select future operational scenarios by modifying the ERTL, which opens the possibility of fast-ion control through the application of 3D perturbations. Furthermore, this provides the capability for future studies to optimize the operational scenarios based on the device needs, avoiding a critical degradation of fast-ion confinement while still mitigating plasma fluctuations.

Appendix A

Radial drift due to the variation of P_ϕ

The toroidal canonical momentum of a charged particle in a magnetic field is given by:

$$P_\phi = -eZ\Psi + mRv_\phi \tag{A.1}$$

Considering a variation in P_ϕ between two consecutive points at poloidal angle $\theta = 0°$ where the parallel velocity has de same sign, it reads:

$$\Delta P_\phi = P_{\phi 2} - P_{\phi 1} = -eZ \int_{r_1}^{r_2} \frac{r'B}{q} dr' + mR_0(v_{\phi 2} - v_{\phi 1}) + m(r_2 v_{\phi 2} - r_1 v_{\phi 2}) \tag{A.2}$$

where θ, R_0 and r represent the particle coordinates as shown in figure A.1. Let us assume that between t_1 and t_2 the values do not change much, therefore $\Delta P_\phi \to dP_\phi$.

$$dP_\phi = -eZ \int_{r_1}^{r_2} \frac{r'B}{q} dr' + mR_0 dv_\phi + md(rv_\phi) \tag{A.3}$$

Taking into account that $dv_\phi/dt = 0$ at $\theta = 0$:

$$\frac{dP_\phi}{dt} = -eZ\frac{rB}{q}\frac{dr}{dt} + mv_\phi\frac{dr}{dt} = \left(-eZ\frac{rB}{q} + mv_\phi\right)\frac{dr}{dt} \tag{A.4}$$

Considering that the toroidal velocity of a trapped ion at the midplane can be approximated by its parallel velocity $v_\phi \approx v_\parallel$:

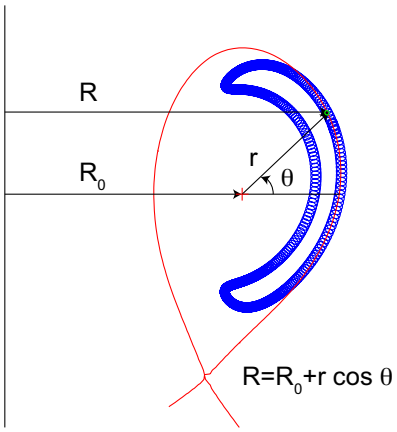

Figure A.1: *Fast-ion trapped trajectory indicating the coordinates corresponding to a generic location P along the orbit.*

$$v_\phi \approx \sqrt{2\epsilon} v_\perp = \sqrt{2\epsilon}\frac{v_\perp}{\omega_c}\omega_c = \sqrt{2\epsilon}\rho\omega_c \tag{A.5}$$

with $\epsilon = r/R$. Here, the parallel velocity was approximated using the upper limit for trapped orbits (i.e. the trapping cone) at $\theta = 0$:

therefore:

$$\frac{dP_\phi}{dt} = eZaB\left(-\frac{r/a}{q} + \sqrt{2\epsilon}\rho_*\right)\frac{dr}{dt} \tag{A.6}$$

where $\rho_* = \rho/a$ and a the plasma minor radius. Assuming the values $r/a \approx 1$ and $q \approx 5$, $\frac{r/a}{q} >> \sqrt{2\epsilon}\rho_*$, equation A.6 can be written as:

$$\frac{dP_\phi}{dt} \approx -eZr\frac{B}{q}\frac{dr}{dt} \tag{A.7}$$

From equation A.7, it follows that a negative variation of P_ϕ is related to an increment of r, leading to a particle drift towards an outer poloidal flux surface.

Author's Contribution

- **Chapter 2: Fast-ions in tokamak.**

  The author produced all figures in this chapter to illustrate the fundamental concepts.

- **Chapter 3: Wave-particle nonlinear resonances.**

  The author has derived an expression for the nonlinear wave-particle interaction by extending the nonlinear resonant theory developed by F. Zonca and L. Chen.

- **Chapter 4: Methodology.**

  The author produced all figures in this chapter to illustrate the most relevant features of the AUG tokamak and the numerical tool ASCOT.

- **Chapter 5: Experimental results.**

  The author has processed and analysed the raw data corresponding to dedicated experiment AUG#33143.

- **Chapter 6: Numerical results.**

  The author has carried out all ASCOT simulations presented in this chapter, post-processed the results and calculated the variation of particle toroidal canonical momentum. The author has also prepared most of the simulation

inputs, including the density and temperatures profiles, modifications of the 3D vessel geometry to include the FILD detector, and magnetic equilibria in vacuum approach.

List of Publications

- **L. Sanchis**, M. Garcia-Munoz A. Snicker, D. A. Ryan, D. Zarzoso, L. Chen, J. Galdon-Quiroga, M. Nocente, J. F. Rivero-Rodriguez, M. Rodriguez-Ramos, W. Suttrop, M. A. Van Zeeland, E. Viezzer, M. Willensdorfer, F. Zonca
"Characterisation of the Fast-Ion Edge Resonant Transport Layer Induced by 3D Perturbative Fields in the ASDEX Upgrade Tokamak through Full Orbit Simulations", Plasma Phys. Control. Fusion, 61, 014038 (2018)

- J. Galdon-Quiroga, M. Garcia-Munoz, K. G. McClements, M. Nocente, M. Hoelzl, A. S. Jacobsen, F. Orain, J. F. Rivero-Rodriguez, M. Salewski, **L. Sanchis-Sanchez**, W. Suttrop, and E. Viezzer,
"Beam-Ion Acceleration during Edge Localized Modes in the ASDEX Upgrade Tokamak", Phys. Rev. Lett., 121, 025002 (2018).

- J. Galdon-Quiroga, M. Garcia-Munoz, **L. Sanchis-Sanchez**, M. Mantsinen, S. Fietz, V. Igochine, M. Maraschek, M. Rodriguez-Ramos, B. Sieglin, A. Snicker
"Velocity space resolved absolute measurement of fast ion losses induced by a tearing mode in the ASDEX Upgrade tokamak", Nucl. Fusion, 58(3), 036005 (2018).

- M. Rodriguez-Ramos, M. Garcia-Munoz, M. C. Jimenez-Ramos, J. Garcia Lopez, J. Galdon-Quiroga, L. Sanchis-Sanchez, J. Ayllon-Guerola, M. Faitsch, J. Gonzalez-Martin, A. Hermann, P. de Marne, J. F. Rivero-Rodriguez, B. Sieglin, A. Snicker
"First absolute measurements of fast-ion losses in the ASDEX Upgrade tokamak", Plasma Phys. Control. Fusion, 59, 10500 (2017)

- M. Garcia-Munoz, S. E. Sharapov, M. A. Van Zeeland, E. Ascasibar, A. Cappa, L. Chen, J. Ferreira, J. Galdon-Quiroga, B. Geiger, J. Gonzalez-Martin, W. W. Heidbrink, T. Johnson, Ph. Lauber, M. Mantsinen, A. V. Melnikov, F. Nabais, J. F. Rivero-Rodriguez, **L Sanchis-Sanchez**, P. Schneider, J. Stober, W. Suttrop, Y. Todo, P. Vallejos, F. Zonca
  "Active control of Alfvén eigenmodes in magnetically confined toroidal plasmas", Plasma Phys. Control. Fusion, 61, 054007 (2019)

Bibliography

[1] IPCC Core Writing Team, R K Pachauri, and L A Meyer. Climate Change 2014: Synthesis Report. *Fifth Assessment Report of the Intergovernmental Panel on Climate Change*, page 151, 2014.

[2] M Salaris and S Cassisi. *Evolution of stars and stellar populations*. Wiley, 2005. ISBN: 978-0-470-09220-0.

[3] International Atomic Energy Agency. Fusion Physics. *International Atomic Energy Agency, Vienna*, 2012.

[4] J Wesson and D J Campbell. *Tokamaks*. Oxford university press, 2004. ISBN: 0-198-50922-7.

[5] J P Freidberg. *Ideal Magnetohydrodynamics*. Kluwer Academic, 1987. ISBN: 978-0306425127.

[6] J P Freidberg. *Plasma physics and fusion energy*. Cambridge University Press, 2007. ISBN: 978-0306425127.

[7] D. A. Spong. *Phys. Plasmas*, 22:055602, 2015.

[8] T C Hender et al. Effect of resonant magnetic perturbations on COMPASS-C tokamak discharges. *Nucl. Fusion*, 32:2091–2117, 1992.

[9] T E Evans et al. Suppression of large edge-localized modes in high-confinement DIII-D plasmas with a stochastic magnetic boundary. *Phys. Rev. Lett.*, 92(23):235003, 2004.

[10] Y Liang et al. Active control of type-I edge-localized modes with n=1 perturbation fields in the JET tokamak. *Phys. Rev. Lett.*, 98:265004, 2007.

[11] W Suttrop et al. First Observation of Edge Localized Modes Mitigation with Resonant and Nonresonant Magnetic Perturbations in ASDEX Upgrade. *Phys. Rev. Lett.*, 106:225004, 2011.

[12] K C Shaing. Symmetry-Breaking Induced Transport in the Vicinity of a Magnetic Island. *Phys. Rev. Lett.*, 87(52):245003, 2001.

[13] K. C. Shaing et al. Transport theory for energetic alpha particles and tolerable magnitude of error fields in tokamaks with broken symmetry. *Nucl. Fusion.*, 54(2):033012, 2014.

[14] C Paz-Soldan et al. Observation of a multimode plasma response and its relationship to density pumpout and edge-localized mode suppression. *Phys. Rev. Lett.*, 114:105001, 2015.

[15] R Nazikian et al. Pedestal Bifurcation and Resonant Field Penetration at the Threshold of Edge-Localized Mode Suppression in the DIII-D Tokamak. *Phys. Rev. Lett.*, 114:105002, 2015.

[16] J-K Park et al. Control of nonaxisymmetric magnetic field perturbations in tokamaks. *Phys. Rev. Lett.*, 99:195003, 2007.

[17] M Willensdorfer et al. Field-line localized destabilization of ballooning modes in three-dimensional tokamaks. *Phys. Rev. Lett.*, 119:085002, 2017.

[18] T Kurki-Suonio et al. Protecting ITER walls: fast ion power loads in 3D magnetic field. *Plasma Phys. Control. Fusion*, 59:014013, 2017.

[19] K Shinohara et al. Effects of complex symmetry-breakings on alpha particle power loads on first wall structures and equilibrium in ITER. *Nucl. Fusion*, 51:63028–12, 2011.

[20] M Garcia-Munoz et al. Fast-ion losses due to high-frequency MHD perturbations in the ASDEX Upgrade tokamak. *Phys. Rev. Lett.*, 100:055005, 2008.

[21] M Garcia-Munoz et al. Convective and diffusive energetic particle losses induced by shear Alfvén waves in the ASDEX Upgrade tokamak. *Phys. Rev. Lett.*, 121:185002, 2010.

[22] J Galdon-Quiroga et al. Beam-ion acceleration during Edge Localized Modes in the ASDEX Upgrade tokamak. *Phys. Rev. Lett.*, 121:025002, 2018.

[23] W W Heidbrink et al. Fast-ion transport by Alfvn eigenmodes above a critical gradient threshold. *Phys. Plasmas*, 24:056109, 2017.

[24] M Garcia-Munoz et al. Fast-ion losses induced by ELMs and externally applied magnetic perturbations in the ASDEX Upgrade tokamak. *Plasma Phys. Control. Fusion*, 55:124014, 2013.

[25] M Garcia-Munoz et al. Fast-ion transport induced by Alfvén eigenmodes in the ASDEX Upgrade tokamak. *Nucl. Fusion*, 51:103013, 2011.

[26] E Hirvijoki et al. ASCOT: Solving the kinetic equation of minority particle species in tokamak plasmas. *Comput. Phys. Commun.*, 185:1310–1321, 2014.

[27] E Speth. Neutral beam heating of fusion plasmas. *Rep. Prog. Phys*, 52:57, 1989.

[28] J Adam. Review of tokamak plasma heating by wave damping in the ion cyclotron range of frequency. *Plasma Phys. Control. Fusion*, 29:442, 1987.

[29] R A Cairns. *Radofrequency heeating in plasmas*. CRC Press, 1991. ISBN: 978-0-750-30034-6.

[30] J-M Noterdaeme. The ASDEX upgrade ICRH antenna. *Fusion Eng. Des.*, 24:67–74, 1994.

[31] J R Cary and A J Brizard. Hamiltonian theory of guiding-centre motion. *Rev. Modern Phys.*, 81.

[32] F Chen. *Introduction to plasma physics and controlled fusion*. Springer, 2007. ISBN: 978-0-444-87475-7.

[33] H Alfvén. On the motion of a charged particle in a magnetic field. *Astron. Fys*, 1:27A, 1940.

[34] T G Northrop. Adiabatic Charged-Particle Motion . *Rev. Geophys*, 1:3, 1963.

[35] H Goldstein. *Classical Mechanics*. Addison-Wesley, 1980. ISBN: 0-201-02918-9.

[36] S I Braginskii. . *Rev. Plasma Phys.*, 1:205, 1965.

[37] F L Hinton, J R, and R D Hazeltine. Theory of plasma transport in toroidal confinement systems. *Rev. Modern Phys.*, 48.

[38] K Kim et al. Numerical verification of bounce-harmonic resonances in neoclassical toroidal viscosity for tokamaks. *Phys. Rev. Lett.*, 110(18):185004, 2013.

[39] K C Shaing, K Ida, and S A Sabbagh. Neoclassical plasma viscosity and transport processes in non-axisymmetric tori. *Nucl. Fusion*, 55:125001, 2015.

[40] H E Mynick. Generalized banana-drift transport. *Nucl. Fusion*, 26(26):491, 1986.

[41] K C Shaing et al. Collisional boundary layer analysis for neoclassical toroidal plasma viscosity in tokamaks magnetohydrodynamic-activity-induced toroidal momentum dissipation in collisionless regimes in tokamaks. *Phys. of Plasmas*, 15(10):082506, 2008.

[42] T E Evans et al. Edge stability and transport control with resonant magnetic perturbations in collisionless tokamak plasmas. *Nat. Physics*, 2:419–423, 2006.

[43] A Loarte et al. Chaos cuts ELMs down to size. *Nat Phys.*, 2:369–370, 2006.

[44] S A Sabbagh et al. Experimental studies of high-confinement mode plasma response to non-axisymmetric magnetic perturbations in ASDEX Upgrade. *Phys. Rev. Lett.*, 97:045004, 2006.

[45] A Bortolon et al. Mitigation of Alfvén Activity in a Tokamak by Externally Applied Static 3D Fields. *Phys. Rev. Lett.*, 110:265008, 2013.

[46] H E Mynick. Transport of energetic ions by low-n magnetic perturbations. *Nucl. Fusion*, 5(26):1471, 1993.

[47] R B White et al. Theory of mode-induced beam particle loss in tokamaks. *Phys. Fluids*, 26:2958, 1983.

[48] X Chen et al. Non-linear wave-particle interactions and fast ion loss induced by multiple Alfvn eigenmodes in the DIII-D tokamak. *Nucl. Fusion*, 54:083005, 2014.

[49] D del Castillo-Negrete, B A Carreras, and V E Lynch. Nondiffusive Transport in Plasma Turbulence: A Fractional Diffusion Approach. *Phys. Rev. Lett.*, 94:065003, 2005.

[50] D Zarzoso et al. Nonlinear interaction between energetic particles and turbulence in gyro-kinetic simulations and impact on turbulence properties. *Nucl. Fusion*, 57:072011, 2017.

[51] W Horton. Drift waves and transport. *Rev. Modern Phys.*, 71:735, 1999.

[52] L Chen et al. Physics of Alfén waves and energetic particles in burning plasmas. 2016.

[53] G J Kramer et al. Fractional Resonances between Waves and Energetic Particles in Tokamak Plasmas. *Phys. Rev. Lett.*, 109:035003, 2012.

[54] F Zonca et al. Nonlinear dynamics of phase space zonal structures and energetic particle physics in fusion plasmas Related content Energetic particles and multi-scale dynamics in fusion plasmas Nonlinear dynamics of phase space zonal structures and energetic particle ph. *New J. Phys.*, 17:13052, 2015.

[55] B Chirikov. Resonance processes in magnetic traps. *J. Nucl. Energy Part C: Plasma Phys.*, pages 1–253, 1960.

[56] F Zonca. Nonlinear physics of shear Alfvén waves. *AIP Conference Proceeding*, 5:1580, 2014.

[57] A J Brizard and T S Hahm. Foundations of nonlinear gyrokinetic theory. *Rev. Modern Phys.*, 79.

[58] A J Lichtenberg and M A Lieberman. *Regular and stochastic motion*. Springer, 1983. ISBN: 978-1-4757-4257-2.

[59] R B White. *Theory of tokamak plasma*. North-Holland, 1989. ISBN: 978-3-319-22308-7.

[60] X Garbet. Instabilits, turbulence et transport dans un plasma magnétisé. *Habilitation dissertation, University of Marseille, France*, 2001.

[61] G E Andrews. *Special functions*. Cambridge University Press, 2013. ISBN: 978-1-107-32593-7.

[62] A Kallenbach. Overview of ASDEX Upgrade results. *Nucl. Fusion*, 47.

[63] W Suttrop, A. Kirk, and others. In-vessel saddle coils for MHD control in ASDEX Upgrade. *Fusion Eng. Des.*, 84(2-6):290–294, 2009.

[64] O Asunta et al. Modelling neutral beams in fusion devices: Beamlet-based model for fast particle simulations. *Comput. Phys. Commun*, 188:33–46, 2015.

[65] A H Boozer and K Kuo-Petravic. Monte Carlo evaluation of transport coefficients. *Phys. fluids*, 24:851–859, 1981.

[66] H Risken. *The Fokker-Planck Equation*. Springer, Berlin, Heidelberg, 1984. ISBN: 978-3-642-96809-9.

[67] W H Press, B P Flannery, S A Teukolsky, and W T Vetterling. *Numerical recipes*. Press Syndicate of the University of Cambridge, 1986. ISBN: 978-05213-8330-1.

[68] A Snicker, S Sipila, and T Kurli-Suonio. Realistic simulations of fast-ion wall distribution including effects due to finite Larmor radius. *IEEE T Plasma Sci*, 38:2177–2184, 2010.

[69] C D Challis et al. Non-inductively driven currents in JET. *Nucl. Fusion*, 29:563, 1989.

[70] R J Goldston et al. New techniques for calculating heat and particle source rates due to neutral beam injection in axisymmetric tokamaks. *Nucl. Fusion*, 43:61–78, 1981.

[71] D Badouel. An efficient ray-polygon intertection. *Graphic gems*, pages 390–393, 1990.

[72] ITER Physics Expert Group on Disruptions, Plasma Control, and MHD and ITER Physics Basis Editors. Chapter 3: MHD stability, operational limits and disruptions. *Nucl. Fusion*, 39:2251, 1999.

[73] M Garcia-Munoz et al. Scintillator based detector for fast-ion losses induced by magnetohydrodynamic instabilities in the ASDEX upgrade tokamak. *Rev. Sci. Instrum.*, 80:10–307, 2009.

[74] W Suttrop et al. Physical description of external circuitry for Resistive Wall Mode controlling ASDEX Upgrade. *36th EPS Conference on Plasma Phys.*, 2009.

[75] W Schneider et al. ASDEX upgrade MHD equilibria reconstruction on distributed workstations. *Fusion Eng. Des.*, 48:127, 2000.

[76] Y Q Liu et al. Feedback stabilization of nonaxisymmetric resistive wall modes in tokamaks. I. Electromagnetic model. *Phys. of Plasma*, 7:3681, 2000.

[77] M Faitsch, B Sieglin, T Eich, A Herrmann, and W Suttrop. 2D heat flux in ASDEX Upgrade L-Mode with magnetic perturbation. *Nuclear Materials and Energy*, 12:225004, 2017.

[78] E Viezzer et al. High-accuracy characterization of the edge radial electric field at ASDEX Upgrade. *Nucl. Fusion*, 53:053005, 2013.

List of Figures

List of Tables